Planes of Satellites around Simulated Disk Galaxies. II. Time-persistent Planes of Kinematically Coherent Satellites in ΛCDM

Isabel Santos-Santos[1] ⓘ, Matías Gámez-Marín[2] ⓘ, Rosa Domínguez-Tenreiro[2,3] ⓘ, Patricia B. Tissera[4,5,6] ⓘ, Lucas Bignone[7] ⓘ, Susana E. Pedrosa[7] ⓘ, Héctor Artal[8] ⓘ, M. Ángeles Gómez-Flechoso[9,10] ⓘ, Víctor Rufo-Pastor[2], Francisco Martínez-Serrano[11] ⓘ, and Arturo Serna[12] ⓘ

[1] Institute for Computational Cosmology, Department of Physics, Durham University, South Road, Durham, DH1 3LE, UK
[2] Departamento de Física Teórica, Universidad Autónoma de Madrid, E-28049 Cantoblanco, Madrid, Spain
[3] Centro de Investigación Avanzada en Física Fundamental, Universidad Autónoma de Madrid, E-28049 Cantoblanco, Madrid, Spain
[4] Instituto de Astrofísica, Facultad de Física, Pontificia Universidad Católica de Chile, Av. Vicuña Mackenna 4860, Santiago, Chile
[5] Centro de Astro-Ingeniería, Pontificia Universidad Católica de Chile, Av. Vicuña Mackenna 4860, 7820436 Macul, Santiago, Chile
[6] Núcleo Milenio ERIS - ANID
[7] Instituto de Astronomía y Física del Espacio, CONICET-UBA, 1428, Buenos Aires, Argentina
[8] Tecplot, Inc., Rutherford, NJ 07070, USA
[9] Departamento de Física de la Tierra y Astrofísica, Universidad Complutense de Madrid, E-28040 Madrid, Spain
[10] Instituto de Física de Partículas y del Cosmos (IPARCOS), Universidad Complutense de Madrid, E-28040 Madrid, Spain
[11] Dassault Systemes S.E., E-28020 Madrid, Spain
[12] Departamento de Física Aplicada, Univ. Miguel Hernández, Elche, Spain

Abstract

We use two zoom-in ΛCDM hydrodynamical simulations of massive disk galaxies to study the possible existence of fixed satellite groups showing a kinematically coherent behavior across evolution (angular momentum conservation and clustering). We identify three such groups in the two simulations, defining kinematically coherent persistent planes (KPPs) that last at least from virialization to $z = 0$ (more than 7 Gyr). This proves that orbital pole clustering is not necessarily set in at low redshift, representing a long-lived property of galaxy systems. KPPs are thin and oblate, represent ∼25%–40% of the total number of satellites in the system, and are roughly perpendicular to their corresponding central disk galaxies during certain periods, consistently with Milky Way $z = 0$ data. KPP satellite members are statistically distinguishable from satellites outside KPPs: they show higher specific orbital angular momenta, orbit more perpendicularly to the central disk galaxy, and have larger pericentric distances than the latter. We numerically prove, for the first time, that KPPs and the best-quality positional planes share the same space configuration across time, such that KPPs act as "skeletons" preventing the latter from being washed out in short timescales. In one of the satellite−host systems, we witness the late capture of a massive dwarf galaxy endowed with its own satellite system, also organized into a KPP configuration prior to its capture. We briefly explore the consequences this event has on the host's KPP and on the possible enhancement of the asymmetry in the number of satellites rotating in one sense or the opposite within the KPP.

Unified Astronomy Thesaurus concepts: Dwarf galaxies (416); Galaxy planes (613); Galaxy kinematics (602); Milky Way Galaxy (1054)

1. Introduction

Planar alignments of satellites observed in the local universe have been considered for a long time as one of the most challenging small-scale issues for Λ cold dark matter (ΛCDM).

Recently, the obtention of proper-motion data for Milky Way (MW) satellites (especially by the Gaia mission) has allowed us to compute their 3D velocities and orbital angular momentum vectors and to study the plane of satellites in the MW as a kinematic structure. Disentangling the clues on the formation of this structure and its stability, in terms of basic physical laws, seems now a more achievable goal than just from spatial data on satellite positions.

The study of positional satellite data alone raised the problem of satellite planes. Later, with the help of numerical simulations, it was possible to evaluate their high significance. Indeed, it was noticed long ago that the "classical" (11 brightest) satellites were arranged in a common planar structure that is approximately perpendicular to the Galactic disk (Lynden-Bell 1976; Kunkel & Demers 1976; Kroupa et al. 2005). In the past decade it has been shown that all known MW satellites fall on the same planar structure, i.e., the so-called "vast polar structure" (VPOS; Pawlowski et al. 2012, 2013). New updates,[13] including ultrafaint satellites, indicate that these add to the VPOS (Santos-Santos et al. 2020b, hereafter Paper I). M31's satellites are also anisotropically distributed (Koch & Grebel 2006; Metz et al. 2007; McConnachie & Irwin 2006), with half of the satellite population forming a thin planar structure, referred to as the "Great Plane of Andromeda" (GPoA; Conn et al. 2013; Ibata et al. 2013; Pawlowski et al. 2013; Santos-Santos et al. 2020b). In addition, a second positional plane of satellites, perpendicular to the former and with comparable population and thickness, was identified in Paper I.

Flattened satellite distributions have also been observed beyond the MW and M31, the best-analyzed system being Cen

---

[13] We caution the reader about possible biases, as the sky has not been homogeneously scanned in search of MW satellites. Most of the newly added ultrafaint galaxies are in the LMC region (e.g., Drlica-Wagner et al. 2015).

A, a massive galaxy with clear signals of a recent merger (see, e.g., Tully et al. 2015; Müller et al. 2016, 2021). Chiboucas et al. (2013), Müller et al. (2017), and Martínez-Delgado et al. (2021) discuss the possibility of flattened satellite distributions around M81, M101, and NGC 253, respectively.

While positional data opened very interesting debates on the issue of satellite planes, the availability of proper motions has opened the possibility of studying them as kinematic entities.

The MW is the only system with 3D kinematic data for a large enough satellite sample that studying these planes as kinematic structures is warranted. Results show that a high fraction of MW satellites present well-aligned orbital poles mostly perpendicular to the Galactic disk axis (Metz et al. 2008; Pawlowski & Kroupa 2013; Gaia Collaboration et al. 2018; Fritz et al. 2018; Pawlowski & Kroupa 2020). Paper I studied the co-orbitation of MW satellites for which kinematic data were available, corresponding to 36 satellites as of 2020 August. Here, as in Paper I, the term "co-orbitation" will mean kinematical coherence no matter the sense of rotation within an aperture $\alpha_{co-orbit} = 36°.87$ (see Fritz et al. 2018). When no distinction is made between one sense of rotation and the contrary within the kinematic structure, it was found that between ~25% and 50% of satellites (taking into account the proper motion uncertainties) show orbital poles within an area of 10% of the sphere around the normal direction to the VPOS. When a distinction is made between co- and counterrotation within the kinematic plane, it was found that the mean fraction of corotating satellites is ~33%. From a total of 36 satellites, this corresponds to 12 satellites, with only four satellites in counterrotation, i.e., a mean ratio of corotating to counter-rotating satellites of 3/1 (and minimum ratio of ~5/3 considering errors; see Figure 11 in Paper I).

While few proper-motion data are currently available for M31 satellites, line-of-sight velocities can be used to elucidate the co-orbitation of M31 satellites forming planes. Ibata et al. (2013) claim a coherent rotational motion of satellites on the GPoA plane seen edge-on from the MW, with the northern satellites receding and the southern ones approaching (see also Sohn et al. 2020). On the other hand, line-of-sight velocities allow us to calculate the perpendicular velocity dispersion of the second positional plane of satellites identified in M31, as it is face-on from the MW: in Paper I it is found to be ~90 km s^{-1}. According to models by Fernando et al. (2017), planes with a perpendicular velocity dispersion above ~50 km s^{-1} dissolve, ending up with half their initial number of satellites in 2 Gyr. Thus, M31's second plane would not be a stable structure. These results, however, should be taken with caution, as distance data for M31 satellites are still uncertain and method dependent. Therefore, the existence of a second positional plane in M31 still has to be confirmed.

Similarly, only line-of-sight velocities are available for the Cen A system. Müller et al. (2018, 2021) discuss the coherent structure of these velocity fields, possibly implying a rotating plane of satellites seen edge-on.

There have been numerous theoretical studies within the ΛCDM cosmological framework addressing the frequency and origin of positionally detected planar alignments of satellites like those observed. These have made use of cosmological simulations, either "dark matter only (DMO)" (Libeskind et al. 2005, 2009; Lovell et al. 2011; Wang et al. 2013; Bahl & Baumgardt 2014; Ibata et al. 2014; Buck et al. 2015, 2016; Cautun et al. 2015; Sawala et al. 2022) or including

hydrodynamics (Gillet et al. 2015; Ahmed et al. 2017; Maji et al. 2017; Garaldi et al. 2018; Shao et al. 2019; Samuel et al. 2021). Positionally detected planes of satellites as thin as the classical plane in the MW, or the GPoA plane in M31, can be found in ΛCDM but are rare. For example, in their analysis of the Illustris simulations, Forero-Romero & Arias (2018) focus on satellite systems within Local Group–like analogs, finding an important dependence on the particular properties of the systems and their evolution, with only 4% of systems similar to the MW one.

Some studies have also investigated the kinematical coherence of satellite planes. Gillet et al. (2015) and Buck et al. (2016) found that good-quality, positionally detected planes at $z = 0$ are not fully kinematically coherent, but only ~30%–60% of their members are. Ahmed et al. (2017) found consistent results in their analysis of four $z = 0$ halos where thin positional planes were detected: only two of these planes had satellite members whose orbital poles clustered (either on a side or the opposite in a spherical projection, meaning that they co-orbit). Santos-Santos et al. (2020a, hereafter Paper II) searched for positional planes of satellites in two different zoom-in hydro simulations along cosmic evolution, using a method based on the "4-galaxy-normal" density plot (Pawlowski et al. 2013). They found, at each time step, planes as thin as and thinner than those observed, whose quality (measured by thinness and population) changes with time. They also found that, in general, the number of co-orbiting satellites is just a fraction of the total number of satellites in the plane, this fraction changing abruptly with time as well. In agreement with previous work, the results from Paper II suggested that high-quality positionally detected planes are unstable, transient structures, probably due to the presence of an important fraction of satellites whose membership is short-lived. These fortuitous interlopers leave or join the structure on short timescales, giving rise to important fluctuations in the positional-plane properties as a function of time.

Instead of focusing on co-orbitation within planes identified in positions, certain works have directly analyzed satellite clustering in angular momentum space. Garaldi et al. (2018) studied four galactic systems, finding groups of satellites with clustered orbital angular momenta in two of them. These groups included up to ~50% of the total number of satellites. Interestingly, these two systems have well-defined central *disk* galaxies. In addition, both satellite groups define thin planes, but the kinematical coherence of satellites sets in at early times in one system (where the ratio of satellites orbiting in one sense to those rotating in the opposite sense is ~7/3) and at late times in the other (where all satellites rotate in the same sense). Other studies have tried to recover the specific kinematical coherence of the MW's "classical" satellites, where 8 out of 11 satellites corotate. Shao et al. (2019) find that only ~30% of all the thin planes with 11 members in the EAGLE volume show such a coherence, and that orbital pole clustering is tighter on average at low redshift, suggesting that kinematic structures like that of the MW may be dynamically young and have formed recently. Sawala et al. (2022) reached similar conclusions on the instability of the MW's plane from satellite orbit integrations using recent proper-motion data (see also Maji et al. 2017; Lipnicky & Chakrabarti 2017). Finally, a new ingredient in the issue of kinematical coherence is introduced by Samuel et al. (2021), who propound that the effect of an LMC-like galaxy on the satellite system favors the thinness and coherence of planes

(see also Garavito-Camargo et al. 2021). However, they also claim that the observed MW plane is likely to be a temporary configuration that will disappear as soon as the LMC moves far away on its orbit.[14]

Finally, other studies focus on external systems beyond the Local Group. In their search of Cen A analogs in the Illustris-TNG simulation, Müller et al. (2021) find 0.2% of them. However, these are not co-orbiting systems but short-lived, chance projections along the line of sight.

From this brief summary about previous results on satellite kinematical coherence, we see that there is a lively debate on this issue, where most authors so far have found that positionally detected planes in ΛCDM simulations do not fully consist of co-orbiting satellites, but only approximately half of them are: that is, positional planes could consist of a fraction of coherently rotating satellites, plus others that have unclustered orbital poles and that, fortuitously, happen to be plane members for a short period. However, previous results are inconclusive with regard to the role that kinematic support can play in ensuring the stability and long-term duration of such planes, the age at which a system acquired its fraction of co-orbitation coherence, and whether or not it persists once acquired.

Indeed, the existence in a system of a subset of satellites that maintains a coherent kinematical behavior over a long period of time is yet to be proven. Should this happen, this subset of coherently orbiting satellites would contribute a kind of skeleton ensuring a long-term durability to positional planes (as suggested by Gillet et al. 2015; Buck et al. 2016). In this case, transient, nonkinematically coherent satellites would be positional-plane members only while they happen to cross it; afterward, they would be lost to the planar configuration and replaced by other transient members.

Finally, it also remains unclear whether there is need for some extra ingredient favoring plane kinematic and/or rotational coherence, e.g., enhancing a higher fraction of co-orbiting and/or corotating orbits in the same sense.

In conclusion, a step forward in understanding the issue of the origin and possible stability and endurance of satellite planes is their study as kinematic configurations. By extending the analysis to the six-dimensional phase space, we can explore the conservation of satellite orbital angular momentum over long time intervals: if a fraction of their orbital pole directions happen to be clustered and remain so, this could be a key to finding an answer. This is the aim of this paper. We note that satellite orbital angular momentum conservation cannot be taken for granted, as the gravitational field satellites feel is a changing one, suffering the effects of mass accretions onto halos and disks, as well as interactions. Analyzing cosmological simulations is an adequate procedure to elucidate this question.

To address this issue in a systematic and detailed manner, in this paper we study the same simulated galactic systems analyzed in Paper II throughout their evolution. We analyze them paying particular attention to the issues related to satellite orbital angular momentum conservation and the clustering of their orbital pole directions, as well as their consequences. In this way we identify fixed sets of satellites whose orbital angular momenta are conserved over long time intervals and whose orbital poles remain clustered, giving rise to thin, persistent-in-time planes. We shall refer to these planes as kinematically coherent persistent

planes (KPPs). We investigate how kinematically identified plane properties evolve with time and quantify their persistence. We also address in this paper the possibility of a second channel that could enhance kinematical coherence and, more specifically, the fraction of satellites corotating in the same sense, involving the late capture of a massive dwarf endowed with its own (sub) satellite system.

Satellites on a persistent plane suggest a scenario where they could have gained their common dynamics at high redshift, probably in unison with the local configuration of the large-scale structure they are embedded in. This issue will be addressed in a forthcoming paper (M. Gámez-Marín et al. 2023, in preparation).

The paper is organized as follows. Sections 2 and 3 introduce the simulations analyzed and their corresponding satellite samples, respectively, focusing on satellite orbit characteristics. Section 4 is devoted to the identification of stable-in-time axes of maximum satellite co-orbitation, and we present our results on satellite KPP members as well. In Section 5 the properties of KPPs as positional planes are studied. In Section 6 we analyze whether satellites in KPPs have properties that make them a group of satellites that are statistically distinguishable from non-KPP ones. Section 7 is devoted to a brief analysis of the late capture of a massive dwarf carrying its own satellite system. The relationships between KPPs and the best-quality positional planes at fixed satellite number are discussed in Section 8. Finally, results are summarized in Section 9, where we also expose the conclusions reached.

2. Simulations

We study planes of satellites orbiting around simulated isolated massive disk galaxies. The two simulations used in this work are Aq-C$^\alpha$ and PDEVA-5004. They make use of different initial conditions, codes, and subgrid prescriptions, which will thus grant our conclusions independence from the many details of simulation modeling.

The simulations have been chosen based on the following criteria or characteristics: (a) the galactic system contains a central galaxy with a thin stellar and gaseous disk at $z \sim 0$ that presents a large radial extent ($\sim$20 kpc); (b) the central galaxy shows an overall quiet merger history, especially free of major-merger events at late times, i.e., after virialization; (c) the system hosts a numerous ($\sim$30) satellite population around the central galaxy; (d) the simulation presents a high enough mass resolution to allow for a minimum of 50 baryonic particles per satellite ($M_{bar} \sim 10^7 M_\odot$). This is in order to ensure that satellite centers of mass and velocity are computed with sufficient accuracy to analyze angular momentum conservation; see Section 3.2.1.

After a pre-analysis of a set of different zoom-in cosmological hydro simulations, we identified two that met the previous prerequisites. Details of each simulation are explained below.

2.1. Aq-C$^\alpha$

The initial conditions of this simulation come from the Aquarius Project (Springel et al. 2008), a selection of DMO MW-sized halos, formed in a ΛCDM 100 h^{-1} Mpc side cosmological box. In this work we analyze a new resimulation of the so-called "Aquarius-C" halo (hereafter Aq-C$^\alpha$), including the hydrodynamic and subgrid models described in Scannapieco et al. (2005, 2006) with the modification presented in Pedrosa & Tissera (2015). The initial mass resolution of baryonic and dark matter particles is $m_{bar} = 4.1 \times 10^5 M_\odot$ and $m_{dm} = 2.2 \times 10^6 M_\odot$,

---

[14] In their analysis of the DMO Millennium-II simulation, Ibata et al. (2014) had already claimed that the rare (0.04%) systems similar to M31 they found include the infall of a massive halo carrying its own set of satellites.

Table 1
Summary Table for Groups of Kinematically Coherent Satellites Identified in the Simulations by Means of the Scanning of Stacked Orbital Poles Method (see Section 4)

Aq-C$^\alpha$		PDEVA-5004 (1)		PDEVA-5004 (2)
$\Delta_{\rm scan} = 36°.87$	$\Delta_{\rm scan} = 34°$	$\Delta_{\rm scan} = 34°$ or $36°.87$, $1T$	$\Delta_{\rm scan} = 34°$ or $36°.87$, $2T$	$\Delta_{\rm scan} = 34°$ or $36°.87$, 1 or $2T$
506	506	5	40	9
346	346	10	10	13
14	14	11	11	19
341	341	26	26	23
473	478	27	27	20
353	353	29	29	16
474	352	40	28	1 (4/3)
29	29	28	8	
345	345	8	5	
21	349	18 (5/5)	22 (6/4)	
349 (5/6)	21 (6/5)			
478 (5/7)	38 (7/5)			
20 (6/7)	474 (7/6)			

Note. Columns give the satellite IDs ordered according to $N_{\rm co-orb}$ (see text). The scanning apertures $\Delta_{\rm scan}$ used to determine the $\boldsymbol{J}_{\rm stack}$ axes are given in the table headers, where it is also indicated whether one ($1T$) or two ($2T$) stacking time intervals have been considered. IDs colored red stand for satellites that rotate in one same sense within the KPP. Those in black rotate in the contrary sense relative to the former. Numbers in parentheses placed at the ith row give the ratio of satellites rotating in one sense over those rotating in the opposite, for satellites whose IDs are in the first i rows.

respectively, with a cosmological model characterized by $\Omega_m = 0.25$, $\Omega_b = 0.04$, $\Omega_\Lambda = 0.75$, $\sigma_8 = 0.9$, $n_s = 1$, and $H_0 = 73$ km s^{-1} Mpc^{-1}.

A standard two-phase process characterizes the halo mass assembly: first a fast phase where mass growth rates are high, mainly through merger activity, and then a slow phase where they decrease. The halo collapse or virialization, i.e., the time when it gets decoupled from global expansion, happens at a universe age of $T_{\rm vir,AqC} \simeq 7$ Gyr ($z_{\rm vir} \simeq 0.76$). This is an important timescale in halo mass assembly history. In this case, 25% of the mass is accreted after collapse.

This galaxy presents a quiet history from $z \approx 1.5$ to $z \approx 0.18$, where no major mergers occur. Soon after, the main galaxy undergoes a potentially disturbing dynamical interaction, as it captures a massive dwarf (hereafter MD, $M_{\rm bar} \sim 5 \times 10^9 \, M_\odot$) carrying its own satellite system. We use this event in Aq-C$^\alpha$ to study its dynamical effects on the original satellite system. To this end, we analyze the simulation both neglecting and including the MD and its satellites.

Properties of the main galaxy measured at redshift $z = 0.18$ are $M_\star = 7.6 \times 10^{10} \, M_\odot$, $M_{\rm gas} = 5.6 \times 10^{10} \, M_\odot$, $M_{\rm vir} = 1.5 \times 10^{12} \, M_\odot$, and $R_{\rm vir} = 219$ kpc.

2.2. PDEVA-5004

The PDEVA-5004 system comes from a zoom-in resimulation run with the PDEVA code (Martínez-Serrano et al. 2008) of a halo identified in a ΛCDM 10 Mpc per side periodic box, where the following parameters are assumed: $\Omega_\Lambda = 0.723$, $\Omega_m = 0.277$, $\Omega_b = 0.04$, and $h = 0.7$. The PDEVA-5004 system (Doménech-Moral et al. 2012) has been previously studied in several projects, where satisfactory consistency with observational data has been found in all the comparisons addressed (see Paper II and references therein). The mass resolution of baryonic and dark matter particles is $m_{\rm bar} = 3.9 \times 10^5 \, M_\odot$ and $m_{\rm dm} = 1.9 \times 10^6 \, M_\odot$, respectively.

The halo growth history shows again a two-phase process with $T_{\rm vir,5004} \simeq 6$ Gyr. Only 20% of the virial mass is assembled after this time, and no major mergers occur. At

redshift $z = 0$, PDEVA-5004's main galaxy presents the following properties: $M_\star = 3.1 \times 10^{10} \, M_\odot$, $M_{\rm gas} = 8.6 \times 10^9 \, M_\odot$, $M_{\rm vir} = 3.4 \times 10^{11} \, M_\odot$, and $R_{\rm vir} \approx 185$ kpc. It is roughly less massive and smaller than Aq-C$^\alpha$.

3. Satellite Samples

3.1. Satellite Identification

In both simulations we identify satellites at two times, $z = 0$ and $z \sim 0.5$ ($T_{\rm uni} = 8.66$ Gyr for Aq-C$^\alpha$ and 8.68 Gyr for PDEVA-5004). The latter time is used to include satellites that may end up accreted[15] by the disk and do not survive until $z = 0$. We define satellites as all objects with stars ($M_\star > 0$) that are bound to the host galaxy within any radial distance. To prove that a given object is a satellite galaxy (i.e., a bound object), we have computed its orbit.

In the case of Aq-C$^\alpha$, structures and substructures were identified using a friends-of-friends algorithm and the SubFind halo finder (Springel et al. 2001). We used the particle IDs to trace the time evolution of the selected satellites and build merger trees. Satellites in PDEVA-5004 were selected as sets of bound particles using IRHYS,[16] which we then followed in time.

The total number of satellites is 34 (35) in Aq-C$^\alpha$ (PDEVA-5004). Of these, 32 (26) survive until $z = 0$.[17] Relevant satellites to this study will be addressed throughout the paper with an identification code (see, e.g., Table 1). Satellites in Aq-C$^\alpha$ (PDEVA-5004) show baryonic masses in the range of $M_{\rm bar} = 8.5 \times 10^6 \, M_\odot$ to $8.9 \times 10^8 \, M_\odot$ ($M_{\rm bar} = 3.9 \times 10^7 \, M_\odot$ to $1.8 \times 10^8 \, M_\odot$). A discussion on the satellite mass distributions

---

[15] Satellite "accretion" stands for the (total or partial) incorporation of the baryonic satellite mass into the central disk, causing the individual satellite to vanish.

[16] Simulation visualization and analysis tool developed by H. Artal, and recently updated as IRHYS-2 (see Section 7) by V. Rufo-Pastor. Not publicly available.

[17] We note that we have improved our satellite tracking method in Aq-C$^\alpha$, resulting in an extension of the survivability of a few satellites further in time than what was presented in Paper II.
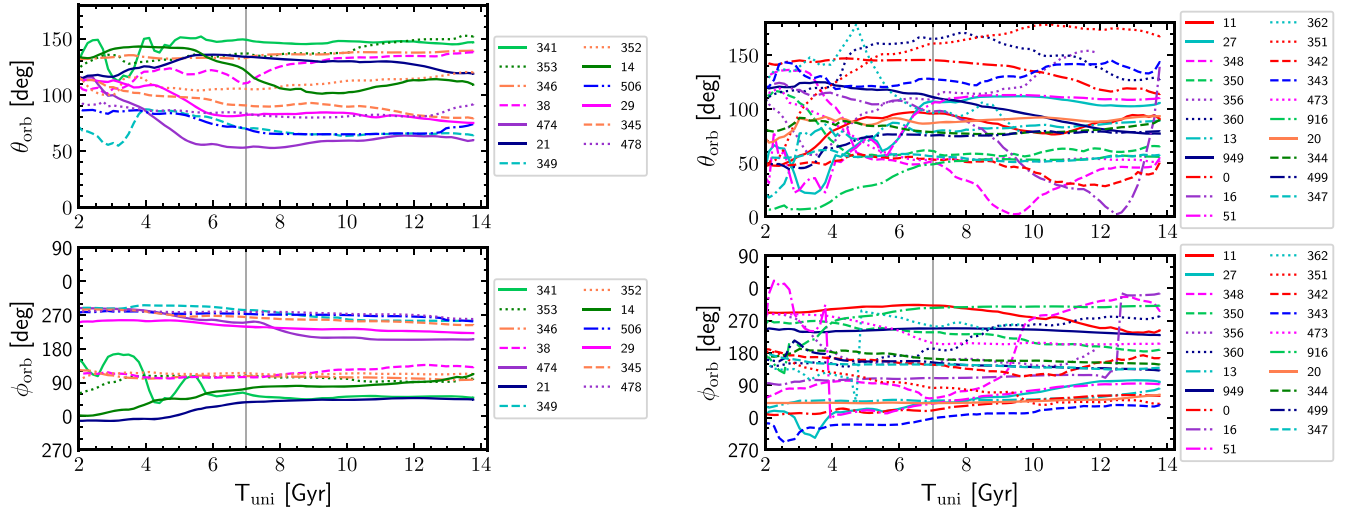
Figure 1. The angular components of the J_{orb} vector of each satellite, as a function of time, for satellites in the Aq-C$^\alpha$ simulation. Satellite samples are divided according to belonging (left panels) or not (right panels) to KPPs; see Table 1, second column. Vertical lines mark the halo virialization time, T_{vir}, i.e., roughly the moment when the halo decouples from cosmic expansion. Satellite IDs are color-coded in the legends.

is given in Paper II, where it is shown that mass is not a property biasing satellite membership to thin planar distributions (see also Collins et al. 2015).

3.2. Orbital Properties

Satellites in both simulations present a diversity of orbital histories. The majority have regular orbits whose apocentric and pericentric distances do not change appreciably during the analyzed time intervals. Some of them show long periods and large apocentric distances, larger than the virial radii in some cases (i.e., backsplash satellites). Finally, a small fraction of satellites see their apocenters gradually reduced as they end up accreted by the central galaxy's disk. Regarding satellites with late incorporations to the system, we find that several Aq-C$^\alpha$ satellites show first pericenters later than $T_{uni} = 10$ Gyr (including the MD), while all of PDEVA-5004's satellites are fully incorporated into the system by that time.

As mentioned in Paper II, a relevant fraction of satellites show pericentric coincidences at some particular cosmic times. In the short periods around these coincidences, an accumulation of satellites occurs at short distances from the main disk galaxy center, enhancing the strength of tidal effects and other possibly disturbing phenomena. Such orbital events may have consequences in the evolution of the individual orbital angular momentum of satellites as we will note throughout the paper. In PDEVA-5004 particularly, several satellites end up accreted by the disk in a short time interval around $T_{uni} \approx 10$ Gyr, after one such pericenter coincidence.

3.2.1. Evolution of the Orbital Angular Momentum with Cosmic Time

We have computed the orbital angular momentum vector J_{orb} of each satellite at each time step. For a given satellite, this is the orbital angular momentum of its center of mass relative to the host disk galaxy's center of mass. Figure 1 shows the time evolution of the directions of J_{orb} vectors (i.e., orbital poles) for the complete satellite set identified in the Aq-C$^\alpha$ simulation. Specifically, we show the evolution starting from high redshift of J_{orb}'s angular components θ, ϕ relative to axes that are kept fixed along cosmic evolution. In the left panels we see that, for many satellites, the orbital

poles are roughly conserved along the slow phase of mass assembly, while this conservation is not that clear for other satellites (see right panels in this figure). Noticeably, T_{vir} is not a particular time concerning orbital pole evolution, as no discontinuity or change of behavior in the orbital pole directions shows up at that moment. Indeed, some satellites roughly maintain their pole directions from $T_{uni} \sim 4$ Gyr onward. At T_{uni} lower than ~ 2 Gyr, most satellite pole directions become noisy, as expected.

It is worth noting that the MD capture happening at $T_{uni} \simeq 11.5$ Gyr does not have a relevant impact on the J_{orb} behavior of the original satellites of the system and, consequently, on the kinematic structures they form (see next sections).

To better illustrate and quantify the information on orbital pole changes, we use Aitoff projections. Figure 2(a) shows the poles of the entire Aq-C$^\alpha$ satellite sample plotted from T_{vir} onward. Satellite identities are coded by colors, and each point stands for a simulation output, i.e., different times. In Figure 2(a) we see that while some satellites have their representative points corresponding to different time steps very close to each other (e.g., satellites #341, 29, 347), others span a large angular distance on the sphere (e.g., satellite #360). The former are examples of satellites whose orbital poles are *conserved*, while the latter do not conserve orbital angular momentum.

In the quest for persistent, kinematically aligned satellite systems, the second necessary ingredient is the *clustering* of a high fraction of conserved poles, belonging to different satellites. Examples of this behavior can also be found in Figure 2(a). We will take advantage of this behavior to determine, in Section 4.1, the axes of maximum satellite co-orbitation.

3.2.2. Satellite Orbital Plane Orientation with Respect to the Central Disk Galaxy

Figure 2(d) shows, for each simulation, the time evolution of the orientation of the central disk galaxy's spin vector, J_{disk}, relative to a fixed reference frame. In the specific case of Aq-C$^\alpha$, in this occasion we use a reference frame that is
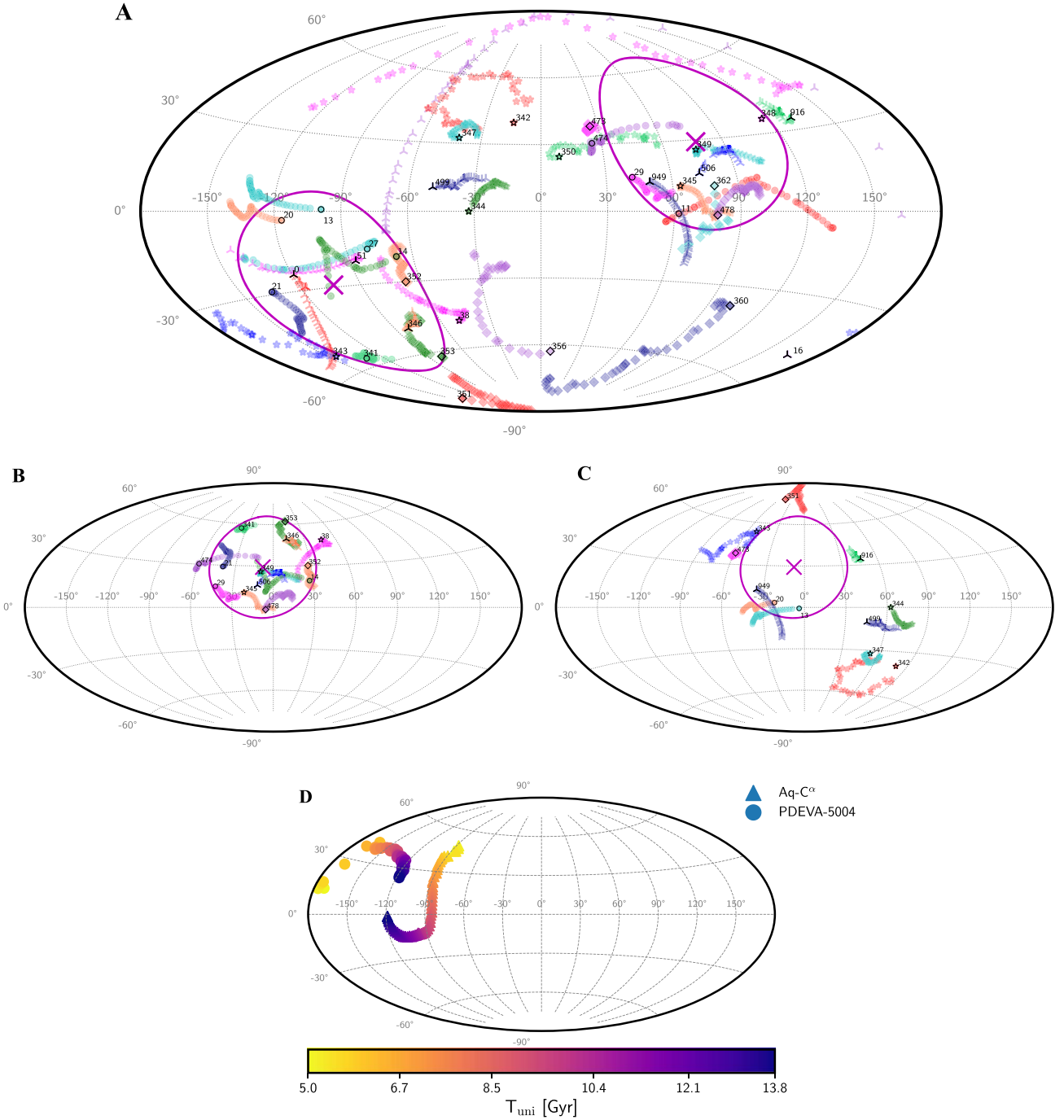
Figure 2. Aitoff projections. (a) Orbital poles (i.e., the J_{orb} directions) for the whole Aq-C$^\alpha$ satellite sample. Satellite identities are specified through point type and color, and different points stand for different output times from T_{vir} to $T_{z=0}$. Satellite ID numbers are given next to their trace point corresponding to $z = 0$. Crosses mark the (axial) axis of maximum satellite co-orbitation, J_{stack}. These crosses are diametrically opposite. The circle around each of them encloses the co-orbiting directions, i.e., those directions at angular distances closer than $\alpha_{co-orbit} = 36°\!.87$ from each axis. Satellites falling within these circles orbit on a common orbital plane, rotating in one sense or in the contrary sense. (b, c) Results of KPP satellite membership determination by means of the stacking method. In these plots only the poles relative to those satellites involved in the stacking procedure are drawn (i.e., those with well-conserved orbital angular momentum; see Section 4.1): (b) satellites belonging to the KPP (second column of Table 1), and (c) satellites outside the former structure. In these panels, J_{orb} are considered as axial vectors and are represented in just one hemisphere. In addition, orbital poles have been rotated 60° in longitude with respect to panel (a) for a clearer visualization. Satellite IDs are specified using the same symbols and colors as in panel (a). (d) Time evolution of the central galaxy's spin vector J_{disk} relative to a fixed reference frame, for both Aq-C$^\alpha$ (triangles) and PDEVA-5004 (circles). Different colors stand for different output times, as encoded in the bar.

oriented such that at high redshift ($z \sim 2.5$; $T_{uni} \sim 2.5$ Gyr) the X-Y plane (located at latitude $\theta = 0°$ in the diagram) contains the protodisk of the central main galaxy.

It is evident that each J_{disk} changes its direction as the simulations evolve. In particular, Aq-C$^\alpha$'s disk axis flips from normal to the X-Y plane at high z to roughly perpendicular to its

former direction, with θ smoothly changing $\Delta\theta \sim 90°$ in all. After that, the host disk remains normal to the formerly mentioned X-Y plane, but rotating very slightly around an axis roughly normal to this plane. In turn, PDEVA-5004's disk spin vector moves very little since T_{vir} and only up to $T_{uni} \approx 10.5$ Gyr.

We have studied the angle formed by J_{orb} and J_{disk} at each time step for all satellites. In both simulations, we have satellites spanning a wide range of $\alpha(J_{disk}, J_{orb})$ values. Angle variations with time are rather smooth in general. Some satellites show long-range patterns in the evolution of $\alpha(J_{disk}, J_{orb})$ that are mainly due to the motions of the disk relative to the fixed reference frame. On the other hand, most satellites that will end up accreted by the disk show a gradual decrease of $\alpha(J_{disk}, J_{orb})$, such that their accretion happens in the plane of the disk. Finally, in both simulations there is an important fraction of satellites with regular, periodic orbital behavior that are on near-to-polar orbits, that is, with $\alpha(J_{disk}, J_{orb}) \sim 90°$. We will study the relative orientation of satellites forming kinematic planar structures in more detail in Sections 5.2 and 6.

4. Identifying Kinematically Persistent Planes of Satellites: Method

Identifying KPPs involves two steps: (i) determining the axes around which the fraction of co-orbiting satellites is a local maximum at each moment within a given time interval, and (ii) identifying the specific, fixed set of satellites that persistently co-orbit these axes along this time interval. We describe our method in the following subsections.

4.1. Identifying Directions of Maximum Satellite Co-orbitation

Scanning over the projections of J_{orb} directions traced on the sphere in search for orbital pole overdensities, at each time step, appears as a direct, straightforward method to look for the direction around which most orbital poles are enclosed within an aperture. However, N_{tot} is generally not high enough for this direct method to converge and produce meaningful results.

As we aim at determining sets of satellites showing orbital pole clustering that is stable along a long interval of time, a second justifiable method consists in considering the satellite poles corresponding to this time interval altogether. That is, for each satellite, its orbital pole directions, corresponding to all the time steps within the period under consideration, are projected on the sphere. Then, we look for clustering in this sample of directions by scanning the sphere just once with a given aperture angle Δ_{scan} in search of an axis around which poles accumulate.

This protocol will be hereafter termed the "Scanning of Stacked Orbital Poles Method," the reason being that, for each satellite, the values of its corresponding orbital poles at each simulation output or time step have been "stacked." By using a stacked sample of orbital poles, the number of J_{orb} directions is multiplied by the number of time steps within the period considered, and convergence in finding clustering is ensured for both simulations.

Note that the longer the periods of time considered, the higher the number of J_{orb} directions to combine together. Ideally, the "stacking" time intervals should be as long as possible. We use as default a stacking interval from T_{vir} to $T_{z=0}$.[18] A limitation to this long period, however, would be the appearance of a dynamical configuration in the system that could possibly spoil or dissolve the stable clustering of a subset of orbital poles. Since we observe such potentially disturbing dynamical events

in both simulations we analyze here, we have considered splitting the default $T_{vir}-T_{z=0}$ range into two subintervals.

In the case of the Aq-C$^\alpha$ simulation, the system is free from suffering potentially disturbing dynamical events until $T_{uni} \sim = 11.5$ Gyr ($z = 0.18$). Soon after, the system enters into an interaction phase, due to the approach and capture of the MD system. In consequence, the $T_{vir}-T_{z=0}$ range has been split into two subintervals separated by $T_{uni} = 11.5$ Gyr. Results obtained using these two time intervals have been compared with those obtained when using the full $T_{vir}-T_{z=0}$ range. As expected from the behavior of satellite orbital poles around $T_{uni} \sim 11.5$ Gyr (i.e., no major impact from the capture; see Figure 1), results for the axes of maximum co-orbitation obtained in either case are essentially the same. Therefore, in what follows we will focus on our results from the analysis of Aq-C$^\alpha$ from T_{vir} to $T_{z=0}$. On the other hand, given the particular dynamical situation the PDEVA-5004 system suffers around 10 Gyr (when several satellites are accreted by the main galaxy), we have considered two stacking subintervals in this case.

To improve the method, some details are in order. Satellites whose orbital pole conservation is not good enough contribute noise (see Section 3.2.1 and Figure 2(a)). In order to minimize noise, satellites that end up accreted by the central galaxy, as well as satellites whose orbital poles sweep an aperture angle higher than $40°$ in the total period analyzed, have been discarded in the stacking procedure. Additionally, in the specific case of Aq-C$^\alpha$, the late-captured MD and its satellites are not included in the stacking procedure because their membership to the system cannot be guaranteed until $T_{uni} \sim 12$ Gyr.

To still increase the local number density of directions and make it easier to identify axes of co-orbitation, in the stacking procedure the satellite orbital poles J_{orb} have been considered as *axial* vectors, i.e., their sense of rotation has not been taken into account. In this case, each of them intercepts twice the unit sphere at diametrically opposite positions, which are indistinguishable for stacking purposes. Hence, the information given in Figure 2(a) can be communicated using a unique hemisphere. As an illustration of our methodology, in panels (b) and (c) of Figure 2 the same information is given using a unique hemisphere, and, additionally, tracks belonging to satellites contributing noise to the stacking procedure have been removed.

The resulting axis of maximum satellite co-orbitation, J_{stack}, identified for the Aq-C$^\alpha$ satellite system, is shown as magenta crosses in Figure 2. The precise location of the J_{stack} axis depends on the scanning aperture Δ_{scan} used. In Figure 2 we plot results for our choice of $\Delta_{scan} = 34°$. Results using a slightly larger value of $\Delta_{scan} = \alpha_{co-orbit} = 36°.87$ have also been analyzed and are very similar (see Section 4.2 and Table 1). Lower Δ_{scan} values have also been explored, but the resulting J_{stack} axes lead to collimated orbital pole groups consisting of a low number of satellites, making them uninteresting for our purposes here. A similar analysis applied to the PDEVA-5004 system returns two J_{stack} axes; see Figure A1 in Appendix A.

Figures 2(b) and (c) show that the J_{stack} axis found indeed points in a direction where the poles of many Aq-C$^\alpha$ satellites cluster. To emphasize these results, panel (b) shows the poles of the KPP satellite members (identified in next Section 4.2), while those satellites not contributing to this structure are drawn in panel (c).

----

[18] We have checked that the maxima in the orbital pole clustering our method returns are robust under extensions of the stacking interval down to $T_{uni} \sim 4$ Gyr.

In Paper I an axis of maximum satellite co-orbation in the MW was determined from kinematic data of satellites at $z = 0$. As no time step stacking is possible in that case, a trick was used that increases the number of directions projected on the sphere, keeping track of the satellite orbital poles' space organization. The so-called "$3J_{orb}$-barycenter method" and its extension to determine KPPs in simulations is described in Appendix B.

4.2. KPP Satellite Membership Determination

Results in the previous subsection indicate that satellite orbital poles cluster in preferred directions. Here we use these co-orbation axes to single out satellites that define KPPs.

To search for and define satellite groups associated with a given J_{stack} axis, we order satellites by decreasing number of time steps within the analyzed period of time, N_{co-orb}, that they cluster around their corresponding J_{stack} axis. That is, N_{co-orb} represents the number of time steps in which a satellite's poles fall within an angle of $\alpha_{co-orbit}$ from the J_{stack} axis, marked with a circle in Figures 2 and A1. To make use of all the available information about pole conservation (see Figure 1), we consider the time interval from $T_{uni} = 4$ Gyr to $T_{z=0}$. The number of satellite members in KPPs has been determined by the criterion that their poles are within the co-orbiting circle for at least 50% of their outputs.[19] This gives 13 satellites in the Aq-C$^\alpha$ KPP and 10 (7) satellite members for KPP1 (KPP2) in PDEVA-5004. In Section 4 we explore whether or not the properties of KPP planes as positional configurations are robust when a more restrictive condition (i.e., a lower number of satellites in KPPs) is imposed.

Table 1 gives the KPP members for Aq-C$^\alpha$. The first (second) column shows results where $\Delta_{scan} = 36°.87$ ($34°$) has been used to determine the stacking axes. Satellite membership differs only very slightly (i.e., just a couple of satellites) between the first and second columns of Table 1.

Satellites whose IDs are colored red in Table 1 rotate in one same sense within the KPP. Those in black rotate in the contrary sense relative to the former. Numbers in brackets at the ith row give the ratio of satellites, among those placed at the first i rows, rotating in the same sense to those rotating in the contrary sense. These ratios change from row to row (i.e., they depend on the number of satellites we take in a given KPP), fluctuating around 50%. However, they further change when including the MD system at $z = 0$; see Section 7.

We proceed in the same way to identify KPP members among PDEVA-5004 satellites. Results are given in the third, fourth, and fifth columns of Table 1. KPP member satellites have been searched for using either a unique stacking interval (results marked $1T$) or two of them, breaking at $T_{uni} = 10.5$ Gyr (marked $2T$). The satellite group corresponding to the main J_{stack} axis (KPP1) differs in just one satellite member between the $1T$ or $2T$ cases. As for the second group (KPP2), it turns out that no differences exist in either the satellite membership or ordering, when one or two stacking intervals are used. Results are given in the fifth column for both cases. Table 1 shows results corresponding to $\Delta_{scan} = 34°$ or $\Delta_{scan} = 36°.87$, as KPP1 and KPP2 satellite members are exactly the same in both cases.

Results obtained by using the "$3J_{orb}$-barycenter method" are given in Table B1. No differences in KPP membership have been found when using one method or the other in the PDEVA-5004 system, and just one satellite varies in the case of Aq-C$^\alpha$. This satisfactory consistency of results using both methods when applied on the two simulations is reassuring and demonstrates that our findings are robust.

These groups of kinematically coherent satellites are candidates to form good-quality *positionally defined* planes. In Section 5 we study the time evolution of their spatial characteristics.

4.3. Quantification of the Degree of Satellite Co-orbation around the Axes Identified

Figure 3 helps us gain a deeper insight into the co-orbation behavior of satellites. In the top panels we show, for three time steps, the fraction of satellites (relative to the whole sample) with orbital poles within a certain angle α measured from the J_{stack} axis, that is, the cumulative distribution function (CDF) for the satellite pole angular distances relative to J_{stack}. In the bottom panels we give the evolution, after the halo collapses at T_{vir}, of the fraction of co-orbiting (within $\alpha_{co-orbit} = 36°.87$) satellites as measured from J_{stack}. Results for Aq-C$^\alpha$ (PDEVA-5004) are shown in the left (right) panels; see legend for details.

A measure of the bias the method gives rise to can be obtained by comparing the difference between orange and gray dotted diagonal lines in the top panels of Figure 3. We see that it is unimportant.

Figure 3 shows that Aq-C$^\alpha$ and PDEVA-5004 present different degrees of orbital pole collimation. In first place, we note that satellite orbital poles in the two simulations are never randomly distributed at small angles (i.e., $< \alpha_{co-orbit}$; $1 - \cos(\alpha) < 0.2$): at any time there is a relevant fraction of "co-orbiting" satellites out of the total. Aq-C$^\alpha$ shows a remarkably high fraction of co-orbiting satellites at all time steps. CDFs exceed the signal for isotropized distributions at 1σ–5σ across different angles. In detail, in the few time steps illustrated, the orbital pole collimation is higher at angular scales $\alpha > 26°$ ($1 - \cos(\alpha) > 0.1$) than at smaller scales.

On the other hand, PDEVA-5004's small-scale degree of collimation is similar for both J_{stack} axes, of around $> 1\sigma$ for $T_{uni} < 9$ Gyr, and of about $> 2\sigma$–3σ at later times. The large-scale collimation ($1 - \cos(\alpha) > 0.5$) is, however, low, showing a distribution compatible with isotropy at some time steps.

We condense the previous results on time behavior in the bottom panels of Figure 3. The fraction of co-orbiting satellites is mostly maintained with only small fluctuations for Aq-C$^\alpha$ with an average of ~ 0.50 (or ~ 0.49 when including the MD system at low z), and reaching higher values at given moments, i.e., approximately half of Aq-C$^\alpha$'s satellite population is co-orbiting on a common orbital plane during the complete period studied. The fraction for both J_{stack} axes in PDEVA-5004 increases as cosmic time evolves. The main (second) co-orbation axis in PDEVA-5004 defines a direction with an average co-orbiting fraction of ~ 0.35 (~ 0.36), that is, in total $\sim 70\%$ of PDEVA-5004's satellites show a high kinematical organization considering both planes, the fraction reaching up to 80% of them at particular times (see black line in the bottom panel). Comparing with the orange line and shaded band in the bottom panels, we see that the clustering of orbital poles at the $\alpha_{co-orbit}$ scale around each J_{stack} direction exceeds that expected from an isotropized distribution. The excess is less

---

[19] This is equivalent to requiring that poles are within the co-orbiting circle for at least half of the time interval we consider.
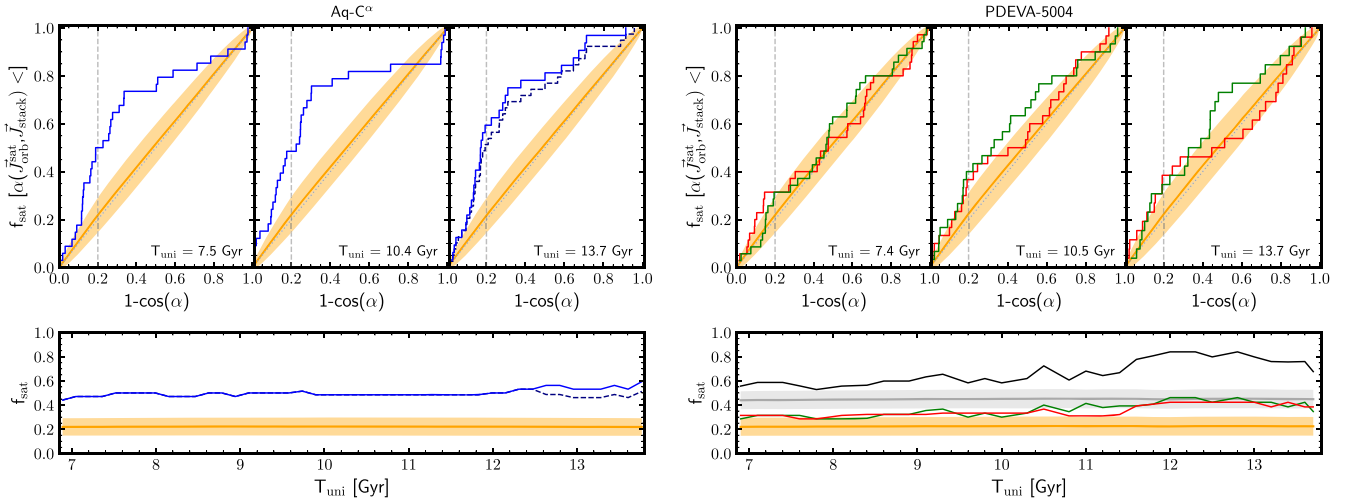
Figure 3. Top panels: fraction of satellites with orbital poles $\boldsymbol{J}_{\rm orb}$ enclosed within an angle α measured from the co-orbitation axes $\boldsymbol{J}_{\rm stack}$, at given time steps. Each panel indicates the universe age $T_{\rm uni}$. Left: Aq-C$^\alpha$; right: PDEVA-5004 (measured from main $\boldsymbol{J}_{\rm stack}$ axis in red, from second axis in green). The orange lines with shaded bands give the results when the method is applied to isotropized configurations of orbital poles (see Appendix C), specifically the averages and 1σ dispersion band over $N_{\rm random} = 5000$ randomized realizations. Gray dotted diagonal lines stand for the analytical result for a homogeneously sampled sphere. A vertical line marks the satellite co-orbitation criterion adopted in this work, i.e., an angle of $\alpha_{\rm co-orb} = 36°.87$ (see text). The dashed line for Aq-C$^\alpha$ represents the situation when including the lately captured MD and its subsatellites. Bottom panels: Time evolution of the fraction of satellites with orbital poles within an angle of $\alpha_{\rm co-orb}$ from the respective $\boldsymbol{J}_{\rm stack}$ axes (i.e., the fraction of "co-orbiting" satellites). For PDEVA-5004, a black line shows the total co-orbiting fraction by summing up contributions from the red and green lines, and a gray line and band indicate the corresponding isotropization mean and scatter to compare it to.

important ($\sim 1\sigma$) for PDEVA-5004 at $T_{\rm uni} \lesssim 9$ Gyr and very relevant for Aq-C$^\alpha$ (some 5σ along the period analyzed).[20]

5. Planes of Kinematically Coherent Satellites

5.1. Qualities of the KPPs

In order to analyze the *quality* of sets of kinematic satellites as planar configurations in position space, we use the standard tensor of inertia (TOI) method (Cramér 1999). Following this approach, an ellipsoid is fitted to the point positions of satellites and a planar configuration results, which can be described by the following:

1. $N_{\rm sat}$: the number of satellites in the subset (or, the fraction of the total number of satellites it represents, $f_{\rm sat} \equiv N_{\rm sat}/N_{\rm tot}$).
2. c/a: the ellipsoid short-to-long-axis ratio.
3. b/a: the ellipsoid intermediate-to-long-axis ratio.
4. $D_{\rm cg}/R_{\rm vir}$: the distance from the center of mass of the central galaxy to the plane, relative to the virial radius (a characteristic total size of the system).
5. $\boldsymbol{n}$: the direction of the normal vector to the planar configuration.

We consider as high-quality planes those that are thin, rather oblate, and populated (i.e., consisting of a relatively high fraction $f_{\rm sat}$ of the total amount of satellites existing at a given time); see Paper II for details.

The TOI analysis has been performed over the whole satellite set listed in Table 1, and then it has been repeated discarding the two last satellites listed there. This is to test whether the 50%

$N_{\rm co-orb}$ criterion to determine the number of KPP satellite members results in sets whose properties in positional space are robust, or a more restrictive condition is needed.

Figure 4 shows some relevant results for the Aq-C$^\alpha$ (left column) and PDEVA-5004 (middle and right columns) simulations. In particular, in the upper block of panels we plot the time evolution, after halo virialization, of the c/a, b/a, $D_{\rm cg}/R_{\rm vir}$, and $f_{\rm sat}$ plane parameters. In the lower block of panels we plot the orientation of the planes. Figure 4 shows that all KPP plane characteristics vary with time (see legends), but not largely. In the case of Aq-C$^\alpha$, the plane remains thin (c/a lower than ~ 0.3) and oblate ($b/a > 0.5$) for the bulk of the period analyzed. Near $T_{\rm uni} \sim 10$ Gyr there is a somewhat larger fluctuation of these parameters, with lower b/a values, but these increase later on. On the other hand, c/a and b/a hardly vary between different $N_{\rm sat}$ groups, confirming that the 50% $N_{\rm co-orb}$ criterion used defines robust structures.

The distance to the central galaxy shows mostly low values (below ~ 10% of the virial radius); however, it shows more fluctuations at different times. We have confirmed that times when $D_{\rm cg}/R_{\rm vir}$ is relatively higher correspond to moments when the satellite distribution is heavily lopsided, with a higher fraction of satellites on one side of the central galaxy than on the other, dragging the fitting plane toward the former side.

Finally, the different $N_{\rm sat}$ groups of Aq-C$^\alpha$ kinematic satellites define planes that are highly populated relative to the total number of satellites of the system. In particular, they represent a fraction of 0.32–0.41 of the total.

PDEVA-5004's main plane of kinematically coherent satellites (shown in red, middle panels) presents as well a remarkable thinness across time, with $c/a \sim 0.2$, and decreasing as time passes. In general, the different quality indicators do not show any relevant fluctuations when $N_{\rm sat}$ changes, an indication of a robust kinematic structure. More particularly, b/a is not that close to unity, suggesting that the KPP is not that oblate as in the case of Aq-C$^\alpha$. $D_{\rm cg}/R_{\rm vir}$ values fluctuate but show overall similar rather low values in both simulations. The kinematically coherent

---

[20] One may examine how these simulated orbital pole distributions and co-orbiting fractions compare to those measured for the MW satellite sample at $z = 0$. We refer the reader to Figure 13 in Paper I. A comparison between simulations and the MW satellite sample shows that results are similar. We note, however, that the MW is different from the simulated galaxies analyzed here in different respects. Therefore, no quantitative agreement should be expected, but just some qualitative similarity as the possible consequence of the same physics.
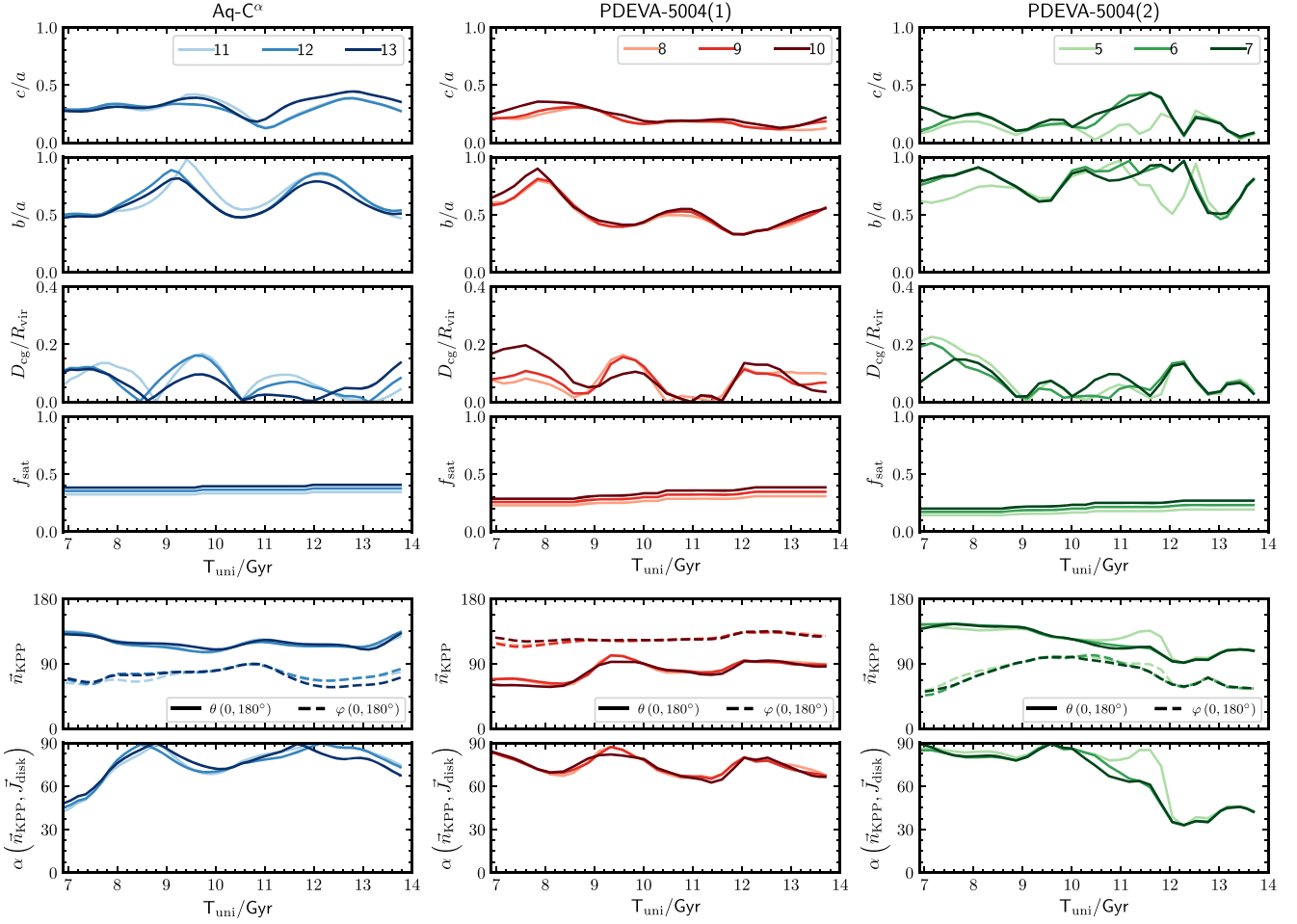
Figure 4. Time evolution of the planes formed by the groups of kinematically coherent satellites identified in each simulation; see Table 1. Left: Aq-C$^\alpha$. Middle: PDEVA-5004 (1) (group corresponding to the main J_{stack} axis). Right: PDEVA-5004 (2) (group corresponding to the second axis). Panels in the upper block show the TOI plane parameters (See Section 5.1). Panels in the lower block show the time evolution of the normal vectors to the KPPs, $\boldsymbol{n}_{KPP}$, in spherical θ, φ angular components with respect to a fixed reference frame, and the angle α formed between $\boldsymbol{n}_{KPP}$ and the spin vector of the central galaxy $\boldsymbol{J}_{disk}$. Colored lines of different shades stand for subsamples of satellites out of the total kinematically coherent group with a different number of satellites N_{sat}, as indicated in the legend, following the N_{co-orb} ordering from Table 1.

satellites represent a maximum fraction of up to $f_{sat} \simeq 0.4$ of the total (for $N_{sat} = 10$), which occurs at late times.

The second group of kinematically coherent satellites identified in PDEVA-5004 gives rise as well to a planar structure in space (shown in green, right panels). The c/a values show more fluctuations than for the main group but are still very low during certain periods, and b/a is always very high, ratifying the oblateness of the structure. Finally, this group represents a maximum fraction of $f_{sat} \sim 0.3$ with $N_{sat} = 7$.

In summary, from Figure 4 it is clear how the subsets of kinematically coherent satellites drawn from either simulation form time-persistent planar configurations, with a good quality during most of the analyzed periods. Furthermore, these KPPs attain a remarkably high quality at some specific time steps.

We finish this subsection by noting that the positional-only analysis presented in Paper II provided higher-quality planes of satellites in both simulations at some redshifts than those presented here (i.e., more populated for equivalent c/a values; see Figure 9 and Table 2 in Paper II). The extra satellites are usually interpreted as transient ones, as mentioned in Section 1. We compare positionally and kinematically identified planes in Section 8.

5.2. Orientation of KPPs

In this section we study the time evolution of the orientation of the KPPs, in relation to (a) a fixed reference frame and (b) the plane of the disk of the central galaxy.

Panels in the lower block of Figure 4 show the evolution of the normal vector to the persistent plane, $\boldsymbol{n}_{KPP}$, in spherical coordinates θ and φ with respect to the fixed reference frame used for each simulation in Section 3.2.1. An outstanding result is that, in both simulations, these orientations or angles do not change appreciably with variations of the number of satellites included in the plane, N_{sat}. Moreover, the $\boldsymbol{n}_{KPP}$ vectors remain approximately fixed in time, with angular components varying steadily and not by much. Indeed, no important fast fluctuations of the direction are found for either simulation.

We also note that all three $\boldsymbol{n}_{KPP}$ directions across time are in rough consistency with their corresponding unique $\boldsymbol{J}_{stack}$ directions.

The panels in the lower block of Figure 4 show the angle formed by the $\boldsymbol{n}_{KPP}$ normal vector and the $\boldsymbol{J}_{disk}$ spin vector of the central galaxy, $\alpha(\boldsymbol{n}_{KPP}, \boldsymbol{J}_{disk})$. Note that, as mentioned in Section 3.2.2 and shown in Figure 2(d), the central galaxies of
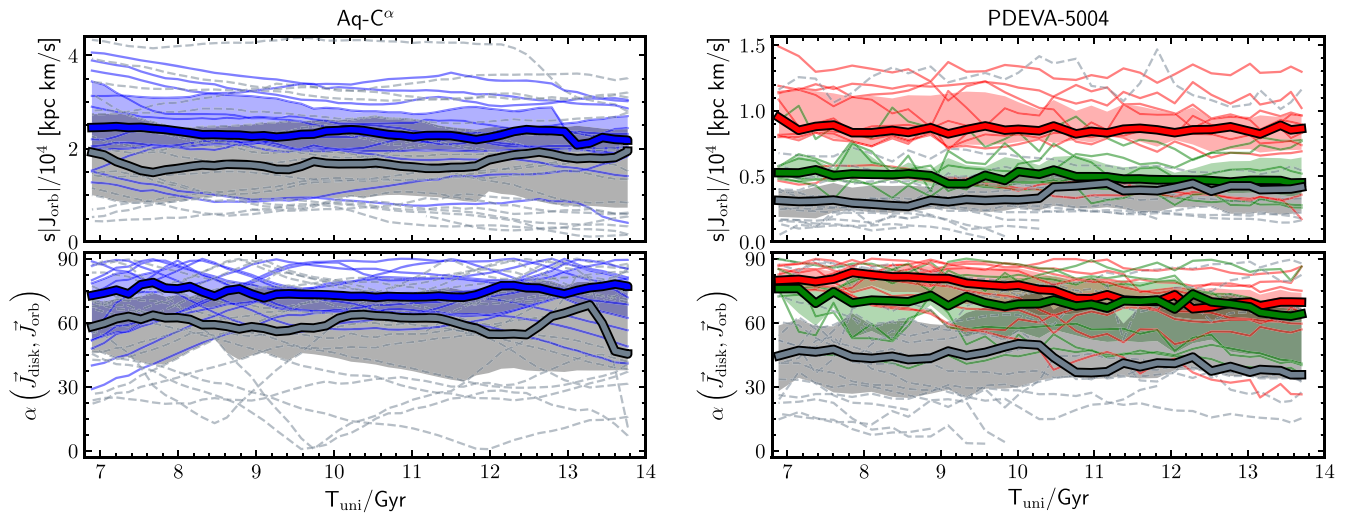
Figure 5. Time evolution of properties of the kinematically coherent satellites identified in each simulation. Left: Aq-C$^\alpha$; right: PDEVA-5004. Top panels show the magnitude of the specific orbital angular momentum $sJ_{\rm orb}$, and bottom panels show the angle formed between the spin vector of the central disk galaxy and the orbital pole of satellites, $\alpha(J_{\rm disk}, J_{\rm orb})$. Thin lines show results for individual satellites, shown in color for kinematically coherent satellites (blue for the main group in Aq-C$^\alpha$, red and green for the main and second groups in PDEVA-5004, respectively), or in dashed gray for nonkinematically coherent ones. Following the same color scheme, a thick line with shade indicates the median and the 25th–75th percentile range, calculated at each time step.

both simulations present their own motions within the fixed reference frame. Thus, these results reflect the combined effect of the motions of the kinematically coherent satellites and of the disk.

In the case of Aq-C$^\alpha$, we find that $\alpha(n_{\rm KPP}, J_{\rm disk})$ increases fast from virialization time until $T_{\rm uni} \approx 9$ Gyr, where it reaches 90°. Beyond this time the central disk galaxy does not vary its orientation relative to the X-Y plane relevantly. By $T_{\rm uni} \sim 11.5$ Gyr, $n_{\rm KPP}$ and $J_{\rm disk}$ become perpendicular again and in general remain roughly so until $z = 0$, with small angle fluctuations therefore only due to minor changes in the orientation of the $n_{\rm KPP}$ vector.

PDEVA-5004's main persistent plane (red, middle column in Figure 4) is also roughly perpendicular to its central disk galaxy during the evolution of the system, showing in general $\alpha > 70°$ and an average angle of $\alpha \sim 80°$ at early times. At $T_{\rm uni} \approx 9.4$ Gyr, the persistent plane is mostly perpendicular to the central galaxy's disk. We recall that PDEVA-5004's disk spin direction changes very little along the analyzed period and therefore the variations found in $\alpha(n_{\rm KPP}, J_{\rm disk})$ are mostly due to fluctuations in the orientation of PDEVA-5004's main $n_{\rm KPP}$ vector. PDEVA-5004's second plane (green, third column in Figure 4) is, interestingly, also remarkably perpendicular to the central disk galaxy at early times. However, after $T_{\rm uni} \sim 10$ Gyr, the perpendicularity is lost and the angle formed with the disk is reduced to $\sim 45°$.[21]

It is noteworthy that both PDEVA-5004's persistent planes are perpendicular to the central galaxy's disk for $T_{\rm uni} < 10$ Gyr. Interestingly, the two planes are also exactly perpendicular to each other at early times, until $T_{\rm uni} \approx 8.5$ Gyr. Afterward, the angle between them decreases drastically (due to the change in direction of the second plane), but then at $T_{\rm uni} \sim 10$ Gyr it starts increasing steadily, reaching an angle of $\sim 70°$ by $z = 0$.

To finish, let us add that no remarkable mutual effects between the spin vector of the central galaxy and the orbital pole directions of satellites (or the normal direction to the

persistent plane) have been appreciated, suggesting that kinematically coherent satellites are least affected by local, secular effects produced by disk changes and may have a cosmological origin. This is consistent with the good conservation of the angular momentum $J_{\rm orb}$ shown by many satellites. We note, however, that their interdependence is unclear from this analysis alone: a study of the total gravitational potential, and of the contribution of the central galaxy's disk to it, would be necessary for a deeper understanding of the role played by the disk in possibly "dragging" the plane of satellites. In principle, satellites will only feel the disk's influence when passing nearby, although the timescale of these close passages may also be important. Such a detailed study is beyond the scope of this work.

6. Properties of Kinematically Coherent Satellites

In order to know whether the kinematically coherent satellites represent a family of satellites with any special common characteristics, differentiating them from the non-kinematically coherent ones, we have analyzed their properties as a group. Particularly, we focus on (i) the magnitude of the satellite-specific orbital angular momentum, $sJ_{\rm orb}$, along time; (ii) the angle formed between the spin vector of the central disk galaxy and the satellite orbital angular momentum vector, $\alpha(J_{\rm disk}, J_{\rm orb})$, along time; (iii) the pericenter distance of satellites to the central disk galaxy, dp, along time; and (iv) the satellite mass. Figure 5 shows the time evolution of $sJ_{\rm orb}$ and $\alpha(J_{\rm disk}, J_{\rm orb})$, for both Aq-C$^\alpha$ (left panel) and PDEVA-5004 (right panel) satellite populations.

Individual lines in the top panels of Figure 5 show that, in the slow phase of mass assembly, $sJ_{\rm orb}$ is overall conserved in many cases.[22] Focusing on the main groups of kinematically coherent satellites of each simulation (blue and red lines), we

---

[21] This change could be triggered by satellite accretion and multiple pericenter coincidences, taking place at similar times. However, this issue is beyond the scope of this work.

---

[22] It is worth noting that the overall values of $sJ_{\rm orb}$ are factors of ~ 2 larger for satellites in Aq-C$^\alpha$ than in PDEVA-5004. The reason is that the halo mass in the former system is a factor of ~ 4 higher than the latter halo mass. High-mass halos collapse later than low-mass ones, and, consequently, acquire higher angular momentum, as predicted by tidal torque theory (see, e.g., López et al. 2019).

can see that they present overall larger sJ_{orb} than the rest of the satellites (dashed gray lines), shown by clearly separated median values across time (except at the very end of the period analyzed for Aq-C$^\alpha$). Kinematically coherent satellites also tend to orbit more perpendicularly to the central disk galaxy than the rest, with larger values of $\alpha(J_{disk}, J_{orb})$ (see bottom panels).

Interestingly, KPP satellites also show significantly larger pericentric distances dp than the rest of satellites: the main groups in Aq-C$^\alpha$ and PDEVA-5004 show a median dp of ~78 (46) kpc in Aq-C$^\alpha$ (PDEVA-5004), versus the ~38 (12) kpc shown by nonkinematically coherent satellites. These results imply that KPP satellites tend to be less affected by disk tidal effects, a factor favoring the long-term conservation of satellite orbital angular momentum.

To confirm quantitatively that the subgroups of kinematically coherent satellites are different from the rest of the satellites in terms of sJ_{orb}, $\alpha(J_{disk}, J_{orb})$, and dp, we have performed statistical Kolmogorov–Smirnov (K-S) tests between the different satellite subsamples. To perform these K-S tests, we have assumed that each satellite contributes to the sample as many times as time steps in which it participates. As an example, if a subsample presents $N_{sat} = 10$ and there are $N_{timesteps} = 40$ time steps in total, we perform the K-S test for that sample with 10×40 elements. We have done these tests for the periods analyzed after halo virialization, i.e., from T_{vir} to $T_{z=0}$, and taking as subsamples the main group of kinematically coherent satellites, on the one hand, and the rest of the satellites of the system, on the other hand. We find that the null hypothesis (i.e., that the two subsamples are drawn from the same underlying population) can be rejected to a higher than 99.9% confidence level, as far as sJ_{orb}, $\alpha(J_{disk}, J_{orb})$, and dp are concerned.

We focus now on the second group of kinematically coherent satellites in PDEVA-5004 (green in Figure 5). Concerning the parameters studied, K-S tests confirm that this group is statistically different from the main group (red). It is also different from the set of satellites that are not associated with either kinematic group (gray), despite the distributions of both samples showing similar medians during some time periods. In this case, kinematically coherent satellites have sJ_{orb} lower than those on the main plane, but still slightly larger than for nonkinematically coherent satellites. These KPP2 satellites also have orbits reaching closer pericentric distances to the central galaxy than those of satellites on the main KPP1 plane. Specifically, we find a median dp of ~22 kpc, only slightly larger than the value for nonkinematically coherent satellites. On the other hand, the angle formed between the orbital plane of satellites and the galactic disk is large, ~70°, slightly lower than but comparable to values found for the main group, evidencing that persistent satellites are not on orbits coplanar with the central disk galaxy.

Finally, in addition to the time evolution of the parameters above, we have also studied the differences between satellites in KPPs and outside them in terms of total baryonic mass. We compare the masses of satellites at a fixed time of $z = 0.5$ for both simulations. In this case, a K-S test shows that it is not possible to reject the null hypothesis. This result agrees with the indistinguishable luminosities and masses observed for M31's on- and off-plane satellites (Collins et al. 2015). It is also consistent with results emphasized in Paper II, where it was found that baryonic mass was not a property driving a higher probability of belonging to high-quality positional

planes of satellites. This finding is relevant, as it shows that the relatively limited mass resolution that current simulations can reach (and therefore limited range of masses found for simulated satellite populations) does not seem to introduce a bias when studying planes of satellites using simulations and comparing the results to observational data (where the mass range spanned may be larger).

7. The Late Capture of a Massive Dwarf Galaxy and Its Subsatellites in Aq-C$^\alpha$

The Aq-C$^\alpha$ system suffers a potentially disturbing dynamical event beginning by $T_{uni} \sim 11.5$ Gyr owing to the late infall of a satellite group. To elucidate whether or not this event affects Aq-C$^\alpha$'s KPP, we had considered different "stacking" time intervals in our analysis in search for KPPs: (i) the entire slow-phase assembly period from T_{vir} to $T_{z=0}$, and (ii) from T_{vir} to $T_{uni} = 11.5$ Gyr. As mentioned in Section 4.1, the directions of the J_{stack} axes found in each case show no remarkable differences. We had concluded that this dynamical event has no perturbing effects on Aq-C$^\alpha$'s KPP.

We now study some details of the dynamical event. Is this a merger or a capture? Are they simple or multiple events? An analysis of the Aq-C$^\alpha$ system beyond $T_{uni} = 11.5$ Gyr through the Subfind halo finder and completed with the recently developed visualization device IRHYS-2 allowed us to identify the capture of an MD galaxy. It has a specific orbital angular momentum relative to the main galaxy with a magnitude of $sJ_{MD, main} \sim 2.2 \times 10^4$ kpc km s^{-1}, conserved since $T_{uni} \sim 7$ Gyr (see Figure 6, right panels, object with ID #836). In addition, the MD's orbital pole with respect to the main galaxy is conserved from $T_{uni} \sim 7$ Gyr onward. At $z = 0$, the MD is at a distance $D_{MD, g} = 65$ kpc from the main galaxy, with the $J_{disk, MD}$ and $J_{disk, main}$ vectors roughly parallel to each other.

This LMC-like galaxy carries six subsatellites (with IDs #907, 837, 838, 839, 840, 841), identified according to the criteria given in Section 3.1.

Their orbital angular momentum relative to the MD galaxy is conserved from high z up to $T_{uni} \sim 12$ Gyr. After this time, angular momentum transfer to the main galaxy begins; see Figure 6. The bottom panel shows an Aitoff projection of the MD's satellite orbital poles, centered on the MD, along the T_{uni} interval between 6.0 and 11.1 Gyr, before this system is captured by the host galaxy. This Aitoff projection shows that five out of six of the subsatellite orbital poles are clustered prior to incorporation: IDs #837, 838, 839, and 841, showing rotation in the same sense, and satellite #907, which is rotating in the opposite sense. Remarkably, not only does the MD galaxy carry its own satellite system, but also this system is kinematically structured, orbiting in a common plane with a high corotating versus counterrotating satellite number ratio (4/1).

Satellites of the MD galaxy system gradually become members of the main galaxy satellite system. The orbital poles of the six MD satellites relative to the main galaxy are roughly conserved from $T_{uni} \sim 12$ Gyr onward (see Figure 6, right panels). One pericentric passage happens for satellites #907 (at 13.3 Gyr) and #841 (at 13.5 Gyr). For the other four satellites, no pericenter relative to the main galaxy has been reached yet before $z = 0$. The same is true for the MD galaxy itself.

As for clustering in orbital pole space at low z, the poles of these seven newly captured satellites span a linear arc in the spherical projection centered on the main galaxy. By $z \sim 0$, three out of the seven newly captured satellites (IDs #836
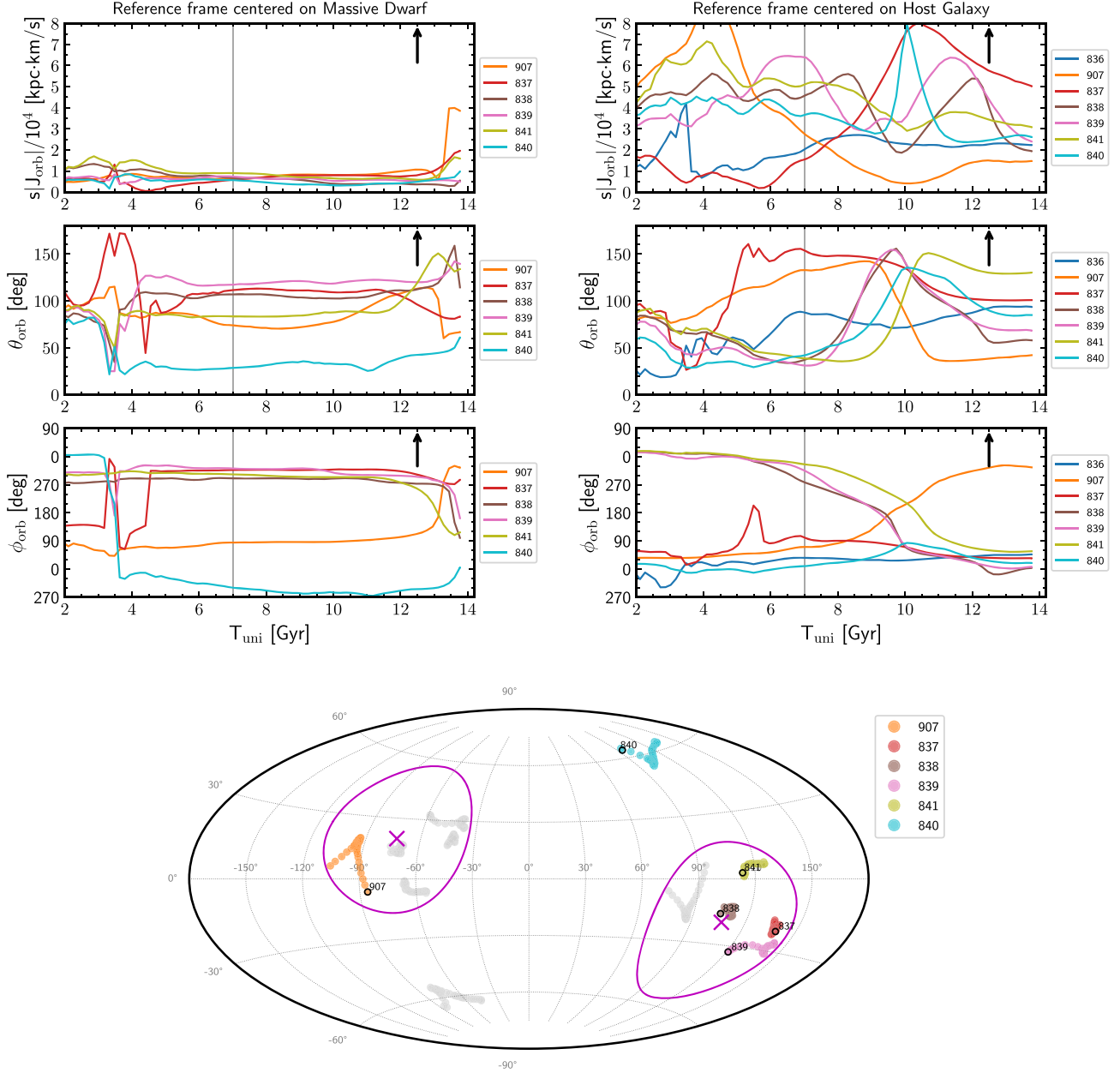
Figure 6. The late capture process of the MD with its own satellite system in Aq-C$^\alpha$. The three upper rows give the components of the J_{orb} vector of each subsatellite, as a function of time, relative to the MD (left panels) and to the main galaxy (right panels). The evolution of the MD's J_{orb} vector relative to the main galaxy is also given in the right panels (ID #836). Vertical arrows mark the capture time ($T_{uni} \approx 12.5$ Gyr), when subsatellites become bound to the host, i.e., the beginning of the time interval along which orbital angular momentum relative to the MD is transferred to the main galaxy. The bottom panel shows an Aitoff projection of the MD's subsatellite orbital poles, centered on the MD, along the T_{uni} interval between 6.0 and 11.1 Gyr, before this system is captured by the host. The corresponding J_{stack} axes are marked with crosses, and circles mark the co-orbitation region. Gray tracks indicate the diametrically opposite projections of each orbital pole, as we consider these as axial vectors in our method (see Section 4.1).

(MD), 837, and 841) are located within the left co-orbitation circle of Figure 2(a) (note that the MD's orbital pole relative to the host galaxy clusters with the original KPP bundle since times much earlier to its capture). This adds three satellites to Aq-C$^\alpha$'s KPP, corotating together with those printed red in Table 1, increasing the ratio of corotating versus counter-rotating satellites from 7/6 to 10/6.[23]

These results show that the late capture of an LMC-like satellite group could have implications in the appearance of highly structured kinematic planes at low z, potentially enhancing asymmetry in the number of satellites rotating in one sense versus those rotating in the contrary sense.

8. Discussion: KPPs versus Positional Planes

Different works have claimed that the highest-quality positional planes one can identify in cosmological simulations are unstable entities, meaning that they lose or change an important fraction of

---

[23] This fraction is consistent with the lower-bound ratio of 5/3 found for the MW in Paper I. However, the wide range of possible ratio values we have obtained prevents us from reaching any strong conclusion about this point.

their satellite members in a short timescale (e.g., Gillet et al. 2015; Buck et al. 2016; Paper II; see Section 1).

Positional planes in Paper II had been selected as the highest-quality ones (i.e., lowest c/a) among those encompassing a fixed fraction of satellites of the whole sample, at a given time (see Figure 9 in Paper II). This selection criterion has as a consequence that the IDs of satellites in these positional structures change from one time output of the simulation to the following, imprinting fluctuations to the curves representing the time evolution of $\alpha(\mathbf{n}, \mathbf{J}_{\mathrm{disk}})$ (the angle formed between the normal vector to the plane, $\mathbf{n}_{\mathrm{pos\%}}$, and the host galaxy's axis). As the number of possible combinations of satellites increases when the fixed fraction of satellites decreases, these fluctuations become more frequent and of higher intensity as the fraction considered decreases.

The angle formed by $\mathbf{J}_{\mathrm{disk}}$ with the normal vector to KPPs is given in the bottom panels of Figure 4 here. In this case, as already mentioned, the evolution curves are rather smooth and do not depend that much on the number of satellites involved, a manifestation of the robustness of KPPs as kinematic entities. In the top panel of Figure 7 we compare the evolution of the angle formed with $\mathbf{J}_{\mathrm{disk}}$ by the normals of both the kinematic planes (magenta curves) and the positional planes as described above (blue curves), for the Aq-C$^\alpha$ sample. We see that the angles formed by kinematic and positional planes evolve in unison, showing their minima and maxima at roughly the same times, and with similar intensity.

This is a necessary condition for the alignment of positional and kinematic normals to occur. We explore such an alignment in the bottom panel of Figure 7.

The best alignments between $\mathbf{n}_{\mathrm{pos\%}}$ and $\mathbf{n}_{\mathrm{KPP}}$ occur when the fraction of satellites involved in positional planes is 90% (depicted by thick dark-blue lines in Figure 7). The number of satellites with which we track KPPs has comparatively a lower impact. We see that, in the 90% case, normals are aligned within an aperture better than $10°$ for roughly half the time interval after T_{vir}. They are aligned to better than $15°$ along the whole interval considered, except for T_{uni} between 9.5 and 11 Gyr and after 13 Gyr. The alignment is worse than $30°$ around $T_{\mathrm{uni}} = 10$ Gyr. In Paper II (see their Figures 6 and 9) we argued that the quality of positional planes in the Aq-C$^\alpha$ set is low along this same time interval. On the other hand, the quality of KPPs as planar structures, including orientation changes, worsens somehow around 10 Gyr as well. A plot of the satellite radial distances to the host center indicates that there is a pericenter accumulation at this epoch, possibly causing these disturbances to positional as well as to kinematic planes. Assessing their causes is beyond the scope of this paper, though.

As said above, when a lower fraction of satellites is used to track positional planes instead, fluctuations become more and more important. With a fraction of 70%, alignments slightly worsen around $T_{\mathrm{uni}} = 8$ Gyr, where, again, the quality of positional planes diminishes; see Figure 6 in Paper II. However, the overall alignment with $\mathbf{n}_{\mathrm{KPP}}$ remains robust qualitatively.

This alignment between normals to KPPs and normals to the best-quality positional planes implies that high-quality positional and kinematically identified planes share the same configurations in positions at fixed times. KPPs constitute a kind of skeleton, persistent along time, to which other satellites add in positions during given limited time intervals. However, the latter are not in coherent kinematic co-orbitation with the former, at least not during long time intervals. Consequently,
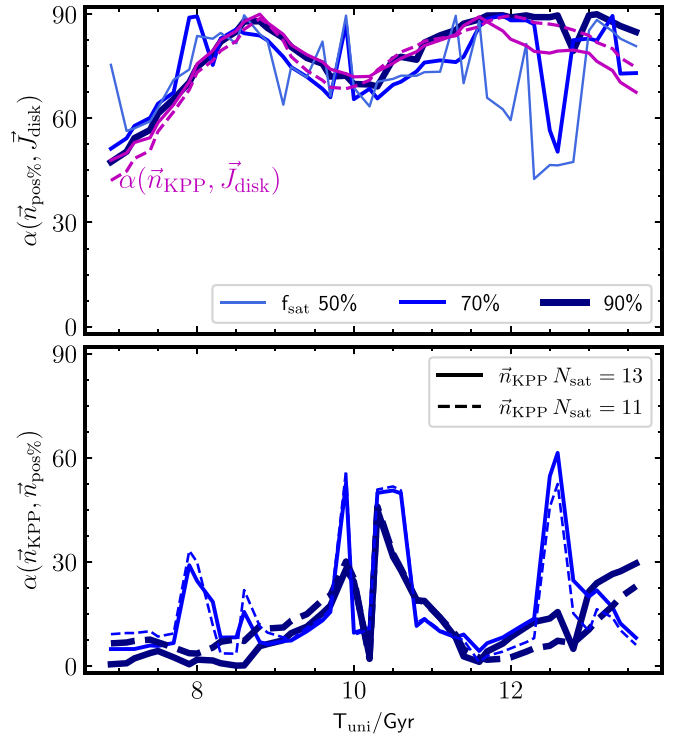

Figure 7. Comparison of the directions of the normals to the KPPs ($\mathbf{n}_{\mathrm{KPP}}$; lower block of panels in Figure 4) with the normals to positional planes ($\mathbf{n}_{\mathrm{pos\%}}$; identified in Paper II), for the Aq-C$^\alpha$ system. The top panels show the angles both normals form with the host disk axis $\mathbf{J}_{\mathrm{disk}}$ along cosmic time. Blue lines refer to the best positional planes involving a given fixed fraction of the total number of satellites. The different shades of these lines stand for these different fractions, as specified in the legends. The magenta lines refer to angles involving the normals to the KPPs, with number of satellites as specified in the legends. In the bottom panel the evolution of the angle formed between the kinematic normals and the positional normals is drawn.

they become lost to the positional configuration after a timescale of the order of the time it takes for each of them to cross the plane.

When the satellite system under consideration has two kinematic planes with similar collimation and intensity, the fluctuations in properties of positional planes described at the beginning of this section become even more important, making it more difficult to implement the analysis we have just made for the Aq-C$^\alpha$ satellite system. This is the case for the PDEVA-5004 system after $T_{\mathrm{uni}} \sim 10$ Gyr. In this case, KPP satellite members of the two kinematic entities are mixed in Figure 9 of Paper II, making it difficult to reach any firm conclusion by applying the protocol described above.

9. Summary and Conclusions

9.1. Summary

In this paper we analyze two zoom-in hydro simulations of disk galaxy formation run in a ΛCDM cosmological context, Aq-C$^\alpha$ and PDEVA-5004, that make use of different initial conditions, codes, and subgrid physics. We identify, in each of them, a skeleton of kinematically coherent, thin planes of satellites, whose member identities persist along ~ 7 Gyr of cosmic evolution at least: the so-called kinematically-coherent persistent planes, or KPPs. By kinematical coherence we mean satellite motions in such a way that their orbital poles are conserved and are clustered for a long period of time, rotating within a common orbital plane in one sense or the opposite.

These identifications are a step forward toward understanding when planes of satellites are set, and whether they can possibly persist along long periods of time or not. We do not intend a detailed comparison to the MW data. The issue of satellite plane persistence is relevant per se and, more importantly, because it could be the consequence of KPP satellites having gained their common dynamics at early times, in unison with the cosmic web local dynamics (M. Gámez-Marín et al. 2023, in preparation). By identifying KPPs, we overcome the drawbacks inherent to methods using three-dimensional satellite positions only, which detect good-quality spatial planar structures, but where only a fraction of satellites are kinematically coherent.

The orbital poles of satellites with good enough orbital angular momentum conservation have been stacked together along time intervals when no relevant disturbing dynamical events occur (from halo collapse—or virialization time—to $z = 0$). Their projection on the sphere has been scanned to look for directions around which the orbital poles accumulate. This protocol has been applied here to the outputs of the two simulations mentioned above, where a massive disk galaxy, radially extended, with a thin disk made of stars and gas, has been identified in each of them.

The analysis returns the directions of stable-in-time axes, $J_{\rm stack}$, around which the number of co-orbiting satellites is maximum: we identify one for Aq-C$^\alpha$ and two for PDEVA-5004. KPP satellite members, corresponding to a given axis $J_{\rm stack}$, have been selected as those whose orbital poles are within an angular distance of $\alpha_{\rm co-orbit} = 36°.87$ from $J_{\rm stack}$ at least for 50% of the simulation outputs. It turns out that the satellite IDs of KPPs this protocol returns are largely the same as those returned by the so-called "3$J_{\rm orb}$-barycenter method"; see Paper I. This is a verification of the robustness of our results.

The groups of KPP satellites are conformed by a relatively high fraction of the total number of satellites in the samples studied in this paper. The fraction is higher in the case of the Aq-C$^\alpha$ KPP ($\sim$40%) and lower in each of the two PDEVA-5004 KPPs, where, when the contributions from the two KPPs are summed up, a fraction as high as $\sim$80% of kinematically structured satellites is found during some time intervals. Within each KPP, the fraction of satellites captured at high z rotating in one sense or the opposite generally tends to be $\sim$50% in either simulation. This situation could be changed by the late capture of a massive dwarf with its own satellite system; see below.

These numbers on co-orbitation are consistent with the fraction of kinematically coherent satellites found in the MW system given the current data uncertainties ($\sim$40%; see Paper I). However, when the sense of rotation is taken into account, the percentage of coherent rotation in the MW is higher (a minimum of 5/3 considering measurement errors; see Paper I).

Planes fitted to the positions of each of these groups of kinematic satellites across time show that KPPs present overall good qualities in terms of a TOI analysis and improve during given time intervals.

The angle formed by the normal to the KPPs and the central galaxy's spin vector, $\alpha(\boldsymbol{n}_{\rm KPP}, \boldsymbol{J}_{\rm disk})$, changes with time, its evolution reflecting the combined effect of disk "flipping" (important in Aq-C$^\alpha$) and the change of orientation of the KPP (not very relevant in either simulation). Curiously in both simulations, the KPPs show an approximately polar orientation with respect to their central disk galaxies over long time periods.

Our results seem to suggest that, contrary to positional planes, the KPPs are little affected by local gravitational forces induced by changes in disk orientation or instabilities. This could imply that they may have a cosmological origin. We note, however, that some changes in the KPPs of the PDEVA-5004 system occur at a moment of multiple satellite pericenter passages and could be due to disk torques on the closest satellites. Exploring these ideas more deeply is outside the scope of this paper.

We have compared the time evolution of the $\alpha(\boldsymbol{n}_{\rm KPP}, \boldsymbol{J}_{\rm disk})$ angle, on the one hand, with that of the angle formed by $\boldsymbol{J}_{\rm disk}$ and the normal to the best-quality positional plane encompassing a fixed fraction of satellites, on the other hand. In the case of the Aq-C$^\alpha$ simulation, these evolutions follow each other. Moreover, the normals to KPPs and those to the positional planes just described are roughly aligned, except in a time interval when an accumulation of satellite pericenters occurs not far from the host galaxy center. This result implies that KPPs and the best-quality positional planes involving fixed satellite fractions are the same configurations in three dimensions in the case of Aq-C$^\alpha$.

As for the PDEVA-5004 system, both their positional and kinematic configurations (with two KPPs) are complex and they mix up, making it difficult to reach any strong conclusion by applying the same protocol as in the previous case.

We have looked for possible indications of a statistically distinguishable behavior between KPP satellites and non-KPP ones. By means of K-S tests, we find that the former are a distinguishable subsample of satellites as compared to the latter regarding the magnitude of their specific orbital angular momentum $sJ_{\rm orb}$, the angles between satellite orbital poles and the host galaxy's spin, and the pericentric distances to the center of the host galaxy. These magnitudes, whose medians show a time dependence, are statistically larger for KPP members than for satellites outside these kinematic structures. These differences are less marked in the case of the second KPP in PDEVA-5004.

Concerning total satellite baryonic mass, K-S tests manifest that the differences are not statistically significant. In other words, at least in these two simulations and within the mass range spanned by satellites, the baryonic mass is not a property that determines whether a satellite belongs or not to the corresponding persistent plane. This is an important result given the limited satellite mass range allowed by current computational possibilities.

9.2. Some Comparisons to Previous Work

To our knowledge this is the first work highlighting the finding and detailed characteristics of ΛCDM-simulated planes of kinematically coherent satellites orbiting around disk galaxies, which are persistent since at least halo virialization.

In a similar fashion to this work, Garaldi et al. (2018) also studied satellite orbital pole clustering, identifying highly populated $z = 0$ planes, including a high fraction of co-orbiting satellites in two out of the four galactic systems they studied, just in those halos containing well-developed spiral galaxies. In one case the satellites maintain clustered orbital poles for a long period of time, with $\sim$1/3 rotating in one sense and 2/3 in the opposite, while in the other case all the satellites rotate in the same sense on a kinematic plane set at recent times. Their c/a results are in

general compatible with those found here for persistent planes in Aq-C$^\alpha$ and PDEVA-5004. However, no systematic searches of co-orbiting satellite groups, studies of satellite membership persistence, or supplementary plane characteristics (e.g., oblateness, orientation) were presented in their work, preventing a proper comparison with our results.

On their part, Samuel et al. (2021) report that, even if rare, they do find, within the $z = 0.2$–0.0 period they analyze, planes as thin and as kinematically coherent as the MW one, including the high fraction of corotating satellites, favored by the presence of LMC-like satellites undergoing pericentric passages.

In line with these ideas, we have studied Aq-C$^\alpha$'s late capture at $T_{uni} \sim 12$ Gyr of a massive dwarf endowed with its own subsatellite system (six satellites, under the selection criterion used in this work). While bound to the massive dwarf (prior to the capture of the system), five out of the six subsatellites co-orbit within a common plane (and four of them rotate in the same sense). Once bound to the host galaxy, three of these new satellites have been found to corotate within the original KPP plane, increasing the ratio of corotation versus counterrotation at $z = 0$ (i.e., adding three red-colored satellites to results in Table 1). These results go in the sense of the findings by Samuel et al. (2021).

9.3. Conclusions

Summing up, these are the main conclusions of this paper:

1. In each of the two simulations analyzed here, specific fixed sets of satellites have been found that are kinematically coherent across the slow phase of mass assembly, forming a KPP of satellites (one in Aq-C$^\alpha$ with 13 satellites, two in PDEVA-5004 with 10 and 7 members, respectively). This is a consequence of an adequately good angular momenta conservation. KPPs show similar common patterns in both simulations, in spite of their different subgrid physics, feedback implementation, etc.

2. These time-persistent kinematically coherent sets of satellites form the (stable-in-time) skeleton of satellite planes around galaxies, preventing them from being washed out on short timescales. We have proven that good-quality positional planes of satellites and KPPs share the same space configuration in three dimensions. Indeed, positionally detected satellite planes consist of the persistent skeleton plus transient satellites that happen to cross the KPP at the time of observation. The latter are positional-plane members during one crossing timescale, being replaced later on by other transient satellites. In this way, positional satellite planes are long-lasting configurations, although unstable ones.

3. Satellites in KPPs and outside these structures are statistically distinguishable, concerning specific angular momentum and pericentric distances (higher and larger in the former than in the latter, respectively). Satellites in KPPs tend to move on nearer-to-polar orbits too. However, mass is not a satellite property that determines its membership to a KPP, within the limits of this work.

4. Our results suggest that a recent accretion of a massive dwarf carrying its own satellite system represents a possible low-redshift channel enhancing KPPs. Indeed, while it is not a necessary condition to form thin planes of long-lasting kinematically coherent satellites, it might contribute, or might even be necessary, to enhance the fraction of satellites rotating in the same sense in KPPs.

The persistent-across-time character of the kinematically coherent planes of satellites suggests that they have been set at high redshift, probably in unison with larger-scale, local cosmic web structures naturally arising in a ΛCDM cosmological context, as suggested with DMO simulations (Libeskind et al. 2012, 2014). Furthermore, the physical behavior of these satellites (distinguishable distributions of specific angular momenta and pericentric distances from those of nonkinematically coherent ones) points to a statistically distinguishable fate once bound to their host.

This paper presents necessary work involved in disentangling the generic consequences of physical laws acting on satellite systems within a ΛCDM context. Specifically, here we have highlighted the generic roles long-term angular momentum conservation and orbital pole clustering play at setting KPPs. How this clustering might have been set at high redshift is analyzed in a forthcoming paper (M. Gámez-Marín et al. 2023, in preparation).

Appendix A
The "Scanning of Stacked Orbital Poles Method" Applied to the PDEVA-5004 Simulation

Figure A1 shows an Aitoff diagram with the projection of PDEVA-5004 satellite orbital poles across time, and the corresponding axes of maximum satellite co-orbitation (see Section 4 and caption of figure for details).

Figure A1. Same content as Figure 2(a), but for the PDEVA-5004 system: Aitoff projection of the stacked orbital poles for the whole set of PDEVA-5004 satellites. Different colors correspond to different satellite tracks. Within a given color, each point corresponds to a simulation output, that is, different values of the universe age, T_{uni}, from T_{vir} to $T_{z=0}$. Two J_{stack} axes are identified, marked with large crosses (KPP1) and plus signs (KPP2). The IDs of satellites in each KPP plane can be read in Table 1. For more details, see descriptions corresponding to Figure 2(a).

Appendix B
The "$3J_{orb}$-barycenter Method" to Determine the Axes of Maximum Co-orbitation

This method was described in Paper I, where it was used on MW satellite $z = 0$ orbital pole data. We refer the reader to this paper for details. We briefly describe here its application to simulations, which consist of many time steps. In this case, the method uses, at each time step, the directions of the barycenters of all the possible spherical triangles that can be formed from the satellite orbital pole projections on the sphere. At each time step, a direction of maximum satellite co-orbitation is identified by scanning the sphere with an aperture Δ_{scan} (as in the "Scanning of Stacked Orbital Poles Method") but on these barycenters, instead of the satellite orbital poles. As a result, an independent axis of maximum co-orbitation is found for each time step. Then, a prescription to ensure the clustering of conserved satellite orbital poles across time is necessary. We adopt the same protocol as that used in Section 4.2, but now considering the different axes obtained at each time step instead of the fixed J_{stack}. Results for KPP satellite membership using this alternative method are given in Table B1.

The differences regarding KPP member identities in the Aq-C$^\alpha$ and PDEVA-5004 systems obtained with the "barycenter" or the "stacking" method can be read by crossing columns in Tables 1 and B1. For Aq-C$^\alpha$ the difference is of one satellite. In the case of PDEVA-5004, both methods give exactly the same KPP1 and KPP2 plane members with 10 and 7 satellites, respectively.

Table B1
Same as Table 1, but for the "$3J_{orb}$-barycenter Method".

Aq-C$^\alpha$	PDEVA-5004 (1)	PDEVA-5004 (2)
349	10	13
353	11	19
346	26	23
506	27	9
341	29	16
14	5	20
21	40	1 (4/3)
29	8 (4/4)	
478	28	
345	18 (5/5)	
474		
343(6/6)		
352 (7/6)		

Appendix C
Isotropy Tests in the "Scanning of Stacked Orbital Poles Method"

The aim of isotropy tests is to prove that the signal we detect, for example in Figure 3, does not come from a bias introduced by the method we use. To this end, the "Scanning of Stacked Orbital Poles Method" is applied to a number N_{random} of isotropized distributions of satellite orbital poles, yielding, at each realization i, the direction of the axis of maximum satellite co-orbitation corresponding to the ith random realization, $J_{stack,i}$.

When using the "stacking" method, the isotropization process is somewhat more involved than usual. Here, time steps are not individually considered, as the "trajectories" of satellite orbital pole projections on the sphere (determined by Newton's laws) have to be taken into account. For this purpose, we proceeded as follows:

1. We assume that the degree of orbital pole conservation of the satellite set to be isotropized is the same as shown in Figure 2(a) for the Aq-C$^\alpha$ set or in Figure A1 for the orbital poles of the PDEVA-5004 system. If $N_{\rm out}$ is the number of stacked-together snapshots used to calculate the $J_{\rm stack}$ axis in a given time interval, we mark the direction on the sphere of the $N_{\rm out}/2$th snapshot for each of the satellites in the set (i.e., its median), $m_{{\rm orb},k}$, where $k = 1, 2, ..., N_{\rm sat}$.

2. We randomly and independently move each of these $m_{{\rm orb},k}$ anchor vectors on the sphere. The set of "trajectory" points belonging to each satellite is moved on the sphere, together with their corresponding anchor direction.

3. The kth satellite's trajectory points are rotated around their corresponding anchor direction $m_{{\rm orb},k}$ by a random angle. We made a different random shot for each satellite trajectory pattern of points.

4. We then use this set of $N_{\rm sat} \times N_{\rm out}$ points to calculate their $J_{{\rm stack},i}$ axis, corresponding to the ith realization.

5. The next step is to calculate $f_i(\alpha)$ at a given time step $T_{\rm uni}$, in the ith realization. To this end, in each realization i, we singled out the orbital poles of the $k = 1, 2, ..., N_{\rm sat}$ satellites at this particular $T_{\rm uni}$, $n_{{\rm orb},k,i}$. Then, we calculate the angles $\beta_{k,i}$ from the $J_{{\rm stack},i}$ axis to the kth direction $n_{{\rm orb},k,i}$ in this particular ith realization. We calculate the corresponding fraction of directions with their $\beta_{k,i}$ angles lower than a given value α, $f_i(\alpha)$.

6. At fixed time steps, we plot the $f_i(\alpha)$ fractions as a function of $1-\cos(\alpha)$.[24]

7. To finish the exercise, we calculate, for each $1-\cos(\alpha)$ bin, the mean and dispersion of the $f_i(\alpha)$ values. Results are shown as orange lines and shaded bands in Figure 3.

ORCID iDs

Isabel Santos-Santos ● https://orcid.org/0000-0001-6054-2897
Matías Gámez-Marín ● https://orcid.org/0000-0002-1979-0941
Rosa Domínguez-Tenreiro ● https://orcid.org/0000-0001-9905-4882
Patricia B. Tissera ● https://orcid.org/0000-0001-5242-2844
Lucas Bignone ● https://orcid.org/0000-0002-4746-1627
Susana E. Pedrosa ● https://orcid.org/0000-0001-8249-4435
Héctor Artal ● https://orcid.org/0000-0002-1408-9478
M. Ángeles Gómez-Flechoso ● https://orcid.org/0000-0002-0692-7187
Francisco Martínez-Serrano ● https://orcid.org/0000-0003-1579-7182
Arturo Serna ● https://orcid.org/0000-0002-6311-2523

---

[24] Our calculations are made within a hemisphere; therefore, $1-\cos(\alpha)$ runs from 0 to 1.

References

Ahmed, S. H., Brooks, A. M., & Christensen, C. R. 2017, MNRAS, 466, 3119
Bahl, H., & Baumgardt, H. 2014, MNRAS, 438, 2916
Buck, T., Dutton, A. A., & Macciò, A. V. 2016, MNRAS, 460, 4348
Buck, T., Macciò, A. V., & Dutton, A. A. 2015, ApJ, 809, 49
Cautun, M., Bose, S., Frenk, C. S., et al. 2015, MNRAS, 452, 3838
Chiboucas, K., Jacobs, B. A., Tully, R. B., & Karachentsev, I. D. 2013, AJ, 146, 126
Collins, M. L. M., Martin, N. F., Rich, R. M., et al. 2015, ApJ, 799, L13
Conn, A. R., Lewis, G. F., Ibata, R. A., et al. 2013, ApJ, 766, 120
Cramér, H. 1999, Mathematical Methods of Statistics (PMS-9) (Princeton, NJ: Princeton Univ. Press), http://www.jstor.org/stable/j.ctt1bpm9r4
Doménech-Moral, M., Martínez-Serrano, F. J., Domínguez-Tenreiro, R., & Serna, A. 2012, MNRAS, 421, 2510
Drlica-Wagner, A., Bechtol, K., Rykoff, E. S., et al. 2015, ApJ, 813, 109
Fernando, N., Arias, V., Guglielmo, M., et al. 2017, MNRAS, 465, 641
Forero-Romero, J. E., & Arias, V. 2018, MNRAS, 478, 5533
Fritz, T. K., Battaglia, G., Pawlowski, M. S., et al. 2018, A&A, 619, A103
Gaia Collaboration, Helmi, A., van Leeuwen, F., et al. 2018, A&A, 616, A12
Garaldi, E., Romano-Díaz, E., Borzyszkowski, M., & Porciani, C. 2018, MNRAS, 473, 2234
Garavito-Camargo, N., Patel, E., Besla, G., et al. 2021, ApJ, 923, 140
Gillet, N., Ocvirk, P., Aubert, D., et al. 2015, ApJ, 800, 34
Ibata, R. A., Ibata, N. G., Lewis, G. F., et al. 2014, ApJL, 784, L6
Ibata, R. A., Lewis, G. F., Conn, A. R., et al. 2013, Natur, 493, 62
Koch, A., & Grebel, E. K. 2006, AJ, 131, 1405
Kroupa, P., Theis, C., & Boily, C. M. 2005, A&A, 431, 517
Kunkel, W. E., & Demers, S. 1976, The Galaxy and the Local Group, Vol. 182 (London: Royal Greenwich Observatory), 241
Libeskind, N. I., Frenk, C. S., Cole, S., et al. 2005, MNRAS, 363, 146
Libeskind, N. I., Frenk, C. S., Cole, S., Jenkins, A., & Helly, J. C. 2009, MNRAS, 399, 550
Libeskind, N. I., Hoffman, Y., Knebe, A., et al. 2012, MNRAS, 421, L137
Libeskind, N. I., Knebe, A., Hoffman, Y., & Gottlöber, S. 2014, MNRAS, 443, 1274
Lipnicky, A., & Chakrabarti, S. 2017, MNRAS, 468, 1671
López, P., Merchán, M. E., & Paz, D. J. 2019, MNRAS, 485, 5244
Lovell, M. R., Eke, V. R., Frenk, C. S., & Jenkins, A. 2011, MNRAS, 413, 3013
Lynden-Bell, D. 1976, MNRAS, 174, 695
Maji, M., Zhu, Q., Marinacci, F., & Li, Y. 2017, ApJ, 843, 62
Martínez-Delgado, D., Makarov, D., Javanmardi, B., et al. 2021, A&A, 652, A48
Martínez-Serrano, F. J., Serna, A., Domínguez-Tenreiro, R., & Mollá, M. 2008, MNRAS, 388, 39
McConnachie, A. W., & Irwin, M. J. 2006, MNRAS, 365, 902
Metz, M., Kroupa, P., & Jerjen, H. 2007, MNRAS, 374, 1125
Metz, M., Kroupa, P., & Libeskind, N. I. 2008, ApJ, 680, 287
Müller, O., Jerjen, H., Pawlowski, M. S., & Binggeli, B. 2016, A&A, 595, A119
Müller, O., Pawlowski, M. S., Jerjen, H., & Lelli, F. 2018, Sci, 359, 534
Müller, O., Pawlowski, M. S., Lelli, F., et al. 2021, A&A, 645, L5
Müller, O., Scalera, R., Binggeli, B., & Jerjen, H. 2017, A&A, 602, A119
Pawlowski, M. S., & Kroupa, P. 2013, MNRAS, 435, 2116
Pawlowski, M. S., & Kroupa, P. 2020, MNRAS, 491, 3042
Pawlowski, M. S., Kroupa, P., & Jerjen, H. 2013, MNRAS, 435, 1928
Pawlowski, M. S., Pflamm-Altenburg, J., & Kroupa, P. 2012, MNRAS, 423, 1109
Pedrosa, S. E., & Tissera, P. B. 2015, A&A, 584, A43
Samuel, J., Wetzel, A., Chapman, S., et al. 2021, MNRAS, 504, 1379
Santos-Santos, I., Domínguez-Tenreiro, R., Artal, H., et al. 2020a, ApJ, 897, 71
Santos-Santos, I. M., Domínguez-Tenreiro, R., & Pawlowski, M. S. 2020b, MNRAS, 499, 3755
Sawala, T., Cautun, M., Frenk, C. S., et al. 2022, MNRAS, in press
Scannapieco, C., Tissera, P. B., White, S. D. M., & Springel, V. 2005, MNRAS, 364, 552
Scannapieco, C., Tissera, P. B., White, S. D. M., & Springel, V. 2006, MNRAS, 371, 1125
Shao, S., Cautun, M., & Frenk, C. S. 2019, MNRAS, 488, 1692
Sohn, S. T., Patel, E., Fardal, M. A., et al. 2020, ApJ, 901, 43
Springel, V., Wang, J., Vogelsberger, M., et al. 2008, MNRAS, 391, 1685
Springel, V., Yoshida, N., & White, S. D. M. 2001, NewA, 6, 79
Tully, R. B., Libeskind, N. I., Karachentsev, I. D., et al. 2015, ApJL, 802, L25
Wang, J., Frenk, C. S., & Cooper, A. P. 2013, MNRAS, 429, 1502